bioRxiv preprint doi: https://doi.org/10.1101/2020.08.23.262048; this version posted August 24, 2020. The copyright holder for this preprint (which was not certified by peer review) is the author/funder, who has granted bioRxiv a license to display the preprint in perpetuity. It is made available under aCC-BY-NC-ND 4.0 International license.

Computational Modeling: Human Dynamic Model

Lijia Liu*, Joseph L. Cooper¤, Dana H. Ballard

1 Department of Computer Science, University of Texas at Austin

* lijialiu@cs.utexas.edu
¤Current Affiliation: Google Inc.

Abstract

Measurements of human activity are useful for studying the neural computations underlying human behavior. Dynamic models of human behavior also support clinical efforts to analyze, rehabilitate, and predict movements. They are used in biomechanics to understand and diagnose motor pathologies, find new motor strategies that decrease the risk of injury, and predict potential problems from a particular procedure. This paper describes a physics-based movement analysis technique for analyzing and simulating bipedal humanoid movements. A 48 degree of freedom dynamic model of humans uses physical simulation software as a tool for synthesizing humanoid movement with sufficient speed and accuracy to allow the analysis and synthesis of real-time interactive applications such as psychophysics experiments using virtual reality or human-in-the-loop teleoperation of a simulated robotic system. The dynamic model is fast and robust while still providing results sufficiently accurate to be used to believably animate a humanoid character, control a simulated system, or estimate internal joint forces used during a movement for creating effort-contingent experimental stimuli. A virtual reality environment developed as part of this research supports controlled experiments for systematically recording human behaviors.

Introduction

The complexity of human motion was first dramatically captured via the Muybridge high-speed photographs [1] which spawned a number of separate analysis techniques in different disiciplines. Visualization first usd keyframing techniques but later sophisticated models used in advanced rendering for computer graphics e.g. [2]. The early cognitive analyses of human behavior [3] focused on human motion in problem solving, using an essentially logical approach. In robotics, sights have been obtained by building physical systems directly [4] that straddle the boundary between humans and robotics that have shed light on the human design. However these efforts are characteristically specialized. In another development, machine learning techniques have been introduced for use in analyzing animal-like motion [5].

Most recent advances in the speed of computing and novel formulations of the dynamic equations of motion have engendered a new approach to understanding human movement fundamentals. Large scale human movement models can be built with the objective of understanding how the human generates goal-oriented behaviors in real time. However the modeling all the complexity of the human musculoskeletal system can be daunting, with over 600 muscles

bioRxiv preprint doi: https://doi.org/10.1101/2020.08.23.262048; this version posted August 24, 2020. The copyright holder for this preprint (which was not certified by peer review) is the author/funder, who has granted bioRxiv a license to display the preprint in perpetuity. It is made available under aCC-BY-NC-ND 4.0 International license.

controlling a complex skeletal system with over 300 degrees of freedom. Moreover to control this complexity, in addition to its vast cortical memory system, the forebrain coordinates specialized subsystems such as the Basal Ganglia and Thalamus in realizing human real-time movement coordination. The upshot is that progress tends to be specialized [6] and there are many open problems [7].

In the face of these complexity challenges, a major alternate modeling route is to forego the level of detail that includes muscles and model more abstract versions of the human system that still use multiple degrees of freedom but summarize muscle effects through joint torques. The computation of the dynamics of such multi-jointed systems recently has also experienced significant advances. The foremost of these, use a kinematic plan to directly integrate the dynamic equations. Several different systems exist, such as MuJoCo, Bullet, Havok, ODE and PhysX, but an evaluation by [8] found them roughly comparable in capability, and only MuJoCo[1] has been applied to human modeling.

Thus there is a need for a exclusively human movement based model that could be used to inform laboratory experiments [9], clinical studies e.g [10] also verify experiments that have only qualitative results [11, 12]. Our human dynamic model (HDM) has a singular focus on human movement modeling and uses a unique approach to integrating the dynamic equations. We have developed a direct dynamics integration method to extract torques from human subjects in real time [13–15] based on a unifying spring constraint formalism.

The system[2] is built on top of the differential equation solver ODE [3], but has significant innovations added in order to handle the closed loop kinematic chains of bipedal movements. Such chains and the contact constraints they introduce have proven difficult to model. Our methodology integrates two key innovations. The first is to allow the kinematic makers of a motion capture system to be modeled as very large point masses.The result is to stabilize the integration of the underlying dynamic equations. The second is to allow the reduction of contact constraints into stiff springs, which has the result of allowing the incorporation of external forces and points of contact.

The lion's share of the computations go towards computing the joint torques from a remembered plan, but there is a balance issue to be dealt with. Human motions for familiar tasks such as balancing while putting on socks rely on remembered protocols, but still need feedback systems such as the vestibular balance system. In the same way simulations with the system show that replaying a set of remembered torques in an open loop manner is delicate as slight kinematic-dynamic mismatches tend to lead to instabilities. We regard this observation as fundamental, biasing our focus towards having motor cortex remembering kinematics of posture changes that can be interpreted by the spinal cord in a closed loop fashion.

The focus of the paper is to describe the HDM simulator as a useful laboratory instrument as well as describe demonstrations that lend support to the kinematic plan approach to movement memory. These goals are illustrated and evaluated in several different demonstrations.

[1] MuJoCo `http://www.mujoco.org/`
[2] Our humanoid mode: `https://github.com/EmbodiedCognition/QtVR`
[3] OpenDE: `http://www.ode.org/`

bioRxiv preprint doi: https://doi.org/10.1101/2020.08.23.262048; this version posted August 24, 2020. The copyright holder for this preprint (which was not certified by peer review) is the author/funder, who has granted bioRxiv a license to display the preprint in perpetuity. It is made available under aCC-BY-NC-ND 4.0 International license.

Model Overview

The HDM model is built on top of the ODE physics engine and is publicly available[4]. The HDM interface, shown in allows the construction of human models using the physics engine via a multi-purpose graphical interface for analyzing movement data captured through interaction with the virtual environment (Fig. 1). With this tool, it is possible to interactively fit a model to marker data, dynamically adjust parameters to test different effects, and visualize the results of kinematic and dynamic analysis, such as the example in Fig 2, which shows a jumping sequence made originally by a human subject and recreated by applying the inverse dynamics method using this tool.

In understanding the model, it helps to appreciate the dynamics engine, which as an innovation in the dynamics integration of formalizing contacts as springs that allow some freedom during the integration. This mathematics is presented here separately in a supplementary information section. The human model takes this integration level for grated. Its separate innovation is recovering the kinematic trajectories of the model joints by mating model points to corresponding motion capture data modeled as large mass idealized points and using springs to force the correspondence.

Any inverse dynamic method h to deal with residual forces [21] owing to unavoidable error sources in the integration process, and our system is no exception. It is instructive to note that the human system has these issues also. Joints have flexible seating, and the dynamic system has to deal with varying loads and terrain. The focus of the human system is balance, given the central importance of its bipedalism. The solution adopted by the HDM is to have a faux auxiliary sensor system that senses deviations of uprightness and generates appropriate correcting forces. Our experiments demonstrate that the resulting residual forces are usually small, on the order of 5%.

Given this introduction, our remaining focus will be to take all of this structure for granted and describe the model's capabilities through a series of examples in different settings.

Test 1: Model validation

Given that the torque recovery technique will be the basis for our experiments, it is essential to establish its accuracy in absolute terms. A straightforward to do this is to use a *particular model* to generate joint torque data and then verify that these generating torques can be recovered with sufficient accuracy. To simulate possible sensor errors in the PhaseSpace system, we introduce noise into the simulated marker positions and study the accuracy of recovery with increasing noise levels.

Synthesized treadmill walking Inverse dynamics computations rely on first finding the model's pose. We tested both steps by studying eight steps of marker data captured from treadmill walking. For this computation, we used data sampled at 60 hz. The movement lasts a little longer than 4 seconds, giving us 260 frames of data. The aim of this study was to assess the effect of sensor noise on the results and compare the joint angles and torques found with our method to those used to generate marker data. We used an experimental process similar to that employed in [23].

[4]Open ODE: `http://www.ode.org/`

bioRxiv preprint doi: https://doi.org/10.1101/2020.08.23.262048; this version posted August 24, 2020. The copyright holder for this preprint (which was not certified by peer review) is the author/funder, who has granted bioRxiv a license to display the preprint in perpetuity. It is made available under aCC-BY-NC-ND 4.0 International license.

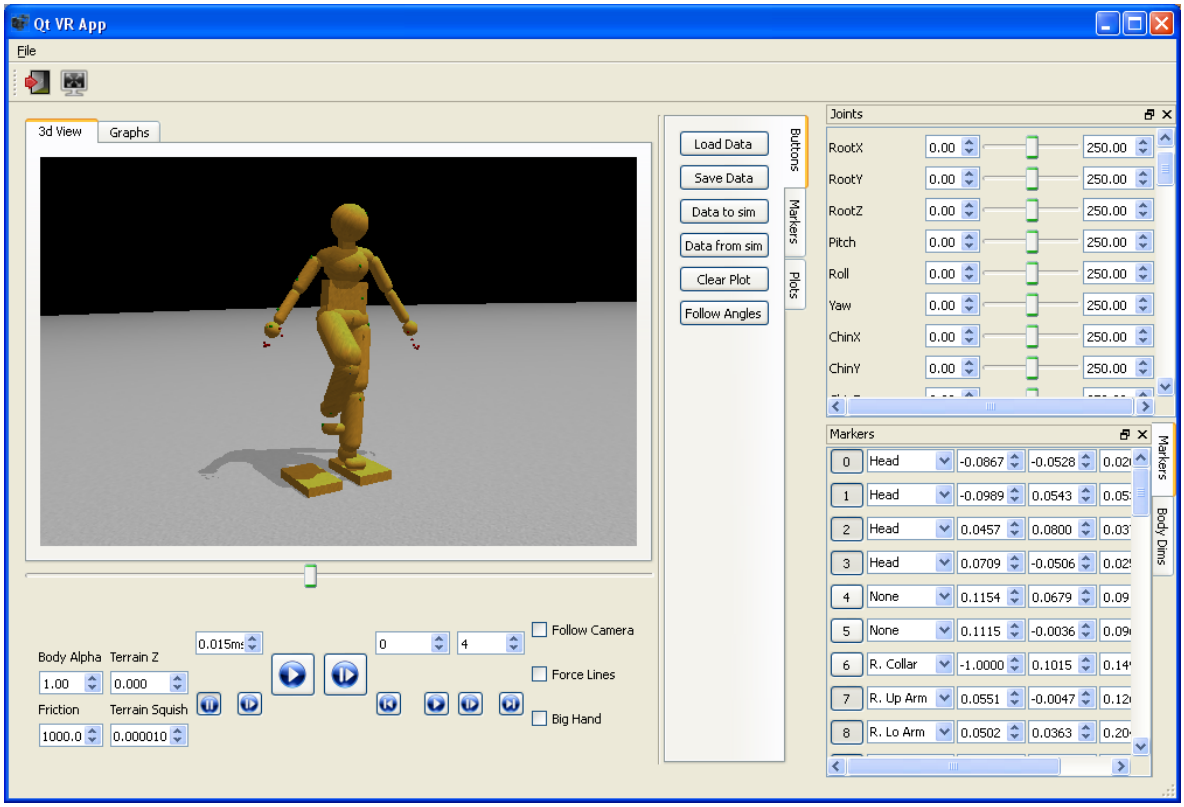

Fig 1. Our analysis tools use the physics engine to compute inverse kinematics and inverse dynamics. They also support various visualizations of relevant data and control for analyzing and producing physically-based movements. The programmed parameters of the model consist of its joints and its 3D marker positions

We used a preliminary pass through the data to generate synthesized "ground truth" marker, pose, and torque data. After using the physics-based inverse kinematics to compute joint angles, we constrained the body to use forward dynamics to reproduce the joint angles with internal torques (and residual forces at the waist segment). As the model performed the movement, we recorded the global position of the marker attachment points. We also recorded the forces used and the resulting joint angles. Thus we had synthetic "ground truth" data directly from the model.

Using the synthetic marker data, we then analyzed the process by perturbing all marker positions at each frame in time along all three axes with mean-centered Gaussian noise of a controlled standard deviation. Applying physics-based pose-fitting followed by inverse dynamics produced a new set of virtual marker positions, joint angles, and torques. The results are shown in Fig 3.

Gaussian perturbations render the marker data dynamically inconsistent. This dynamic inconsistency also pushes a constrained system toward singularity, making it more challenging to solve numerically. We tested with very high levels of noise to see if they would slow the system down, or prevent it from finding any solution. In all cases, the system analyzed the perturbed data in real-time, finding pose data and dynamics data to fit the marker data.

After running through an inverse kinematics pass, an inverse dynamics pass, and a forward dynamics pass for each trial run; we compared the marker attachment points, joint angles, and

bioRxiv preprint doi: https://doi.org/10.1101/2020.08.23.262048; this version posted August 24, 2020. The copyright holder for this preprint (which was not certified by peer review) is the author/funder, who has granted bioRxiv a license to display the preprint in perpetuity. It is made available under aCC-BY-NC-ND 4.0 International license.

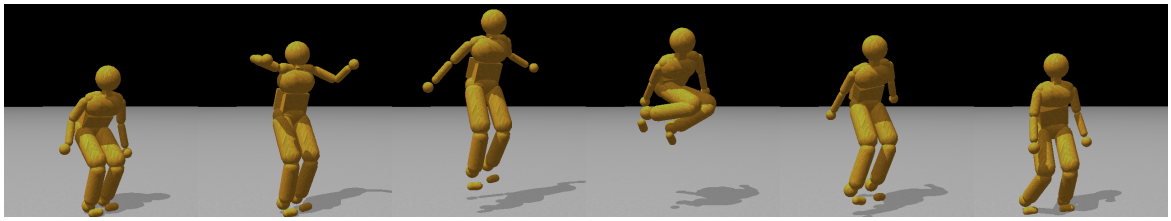

Fig 2. Model capability illustration. A jump sequence reproduced with physics-engine-based inverse dynamics using recorded motion capture data from a human subject. The recreated jump height is achieved completely from ground forces, with small residual torques ($\leq 100Nm$) keeping the model from tipping over.

joint torques from the forward dynamics pass to the synthetic ground truth data. Fig. 3 shows the mean error for across all degrees of freedom and frames of time for each quantity measured. Although the perturbations make the marker data dynamically inconsistent, our results show that small amounts of noise have minimal effect on the computed measurements.

Fig 3 shows that functional recovery is possible with up to 8mm standard error deviations. A ±1mm PhaseSpace marker position accuracy translates in our model into an average joint angle error of 0.02 radians and average force errors of 3 Newtons.

There is a systematic error in both the marker positions and joint angles caused by the fact that the constraints behave like springs. The spring-like behavior causes the marker positions and joint angles to lag behind their targets by a small amount and dampens the overall movement. This lag and damping are apparent in Fig. 4 comparing individual trajectories for selected dimensions of the joint angles and torques. As shown in Fig 4, the data follow ground truth very well under low noise conditions.

Test 2: Residual forces

The Inverse dynamics uses measured kinematics and any external forces to calculate net joint torques in a rigid body linked segment model. [21] However, discrepancies between the dynamic forces of the model and the kinematic of the reality make it so that the dynamic model falls over unless action is taken to stabilize it. Adjustments to internal joint torques can be used to stabilize the body, but cause the body's pose to deviate from its intended pose. A common way to compensate this problem is by introducing 'residual forces and torques' which do not exist in reality. In this work, we used non-realistic external forces to model the effects that would be used by the human vestibular system. We attached a joint to the model's waist to constrain it to reproduce the global orientations found during the pose-fitting pass. To minimize the effect of these external forces, we used torque limits on the amount of stabilizing torque available.

To test how much residual force torque is necessarily relative to the internal joint torques, we obtained movement data together with ground force data from a pair of balance boards. For a simple movement such as transitioning from standing on one foot or the other, residual angular torques of 30Nm were sufficient to keep the dynamic model quite close to its target trajectory. Fig 5 shows the calibration of the ground force computed from our method compared to those taken from Wii^{TM} force plates. A subject standing on two force plates, varied their stance from one being supported exclusively by leg standing on one plate and then shifted their weight to the other leg to be supported by the other plate. During the stance phase, the two measures are in excellent agreement. It compares the sensor-measured ground forces for the right

bioRxiv preprint doi: https://doi.org/10.1101/2020.08.23.262048; this version posted August 24, 2020. The copyright holder for this preprint (which was not certified by peer review) is the author/funder, who has granted bioRxiv a license to display the preprint in perpetuity. It is made available under aCC-BY-NC-ND 4.0 International license.

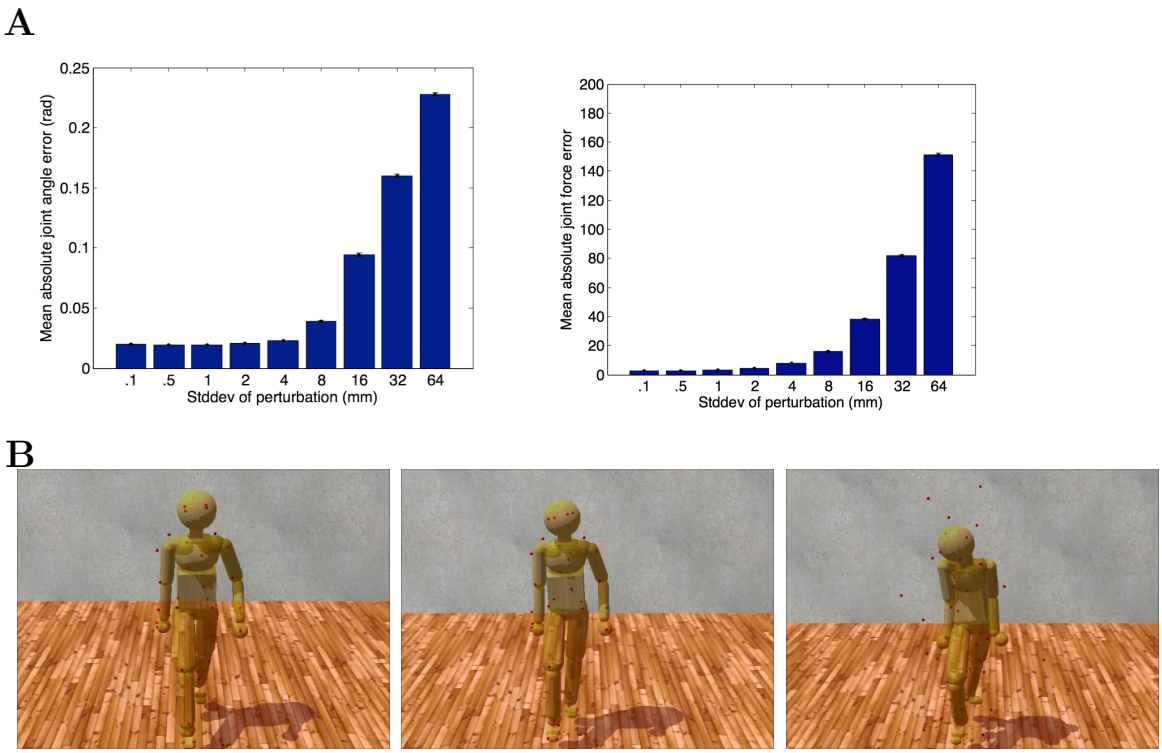

Fig 3. Model noise sensitivity. A.
Error of joint angles, and internal torques resulting from physics-based inverse kinematics and inverse dynamics used to analyze perturbed marker data. We repeated the process twenty times for each noise-level at nine different standard-deviations. Standard-deviations, in mm, were (0.1, 0.5, 1, 2, 4, 8, 16, 32, 64). Error bars show standard error of the mean.(a) The accuracy of the PhaseSpace motion capture device is approximately 5mm over its 3 x 6 meter workspace, resulting an average angular error of 1 degree. (b) The same estimates for torque error are between 5 and 10 Nm, typically approximately 1%. These small errors are well within the requirements for our experiments.**B.** Poses generated by forward dynamics using forces obtained from three inverse dynamics simulations based on Gaussian perturbed walking data (0.1mm, 8mm, and 64mm noise levels). Although at very high levels of noise, the model follows the reference motion poorly, the movement still looks, qualitatively, like walking.

and left feet (red and green lines) to the computed ground forces found through physics-based inverse dynamics (blue and pink lines). Even during bipedal stance, the forces come surprisingly close. The largest discrepancies come during the transition from one foot to the other. These discrepancies can be blamed largely on poor collision detection resulting from an abstract model of the foot.

The figure also shows that the external stabilizing torques are very modest, being within $\pm 5\%$ of the maximum excursion. The correspondence is actually a little better as the faux vestibular balance forces are not factored into the comparison. Note also that we cannot expect the correspondence to be exact during the phase between the two stances as there is no attempt in the model in this test to make the dynamics of the changing stance match that of the force plates.

To generate independent movements, such as grasping might need additional accuracy [22], but for estimating a subject's energetic cost, the accuracy is well within range.

bioRxiv preprint doi: https://doi.org/10.1101/2020.08.23.262048; this version posted August 24, 2020. The copyright holder for this preprint (which was not certified by peer review) is the author/funder, who has granted bioRxiv a license to display the preprint in perpetuity. It is made available under aCC-BY-NC-ND 4.0 International license.

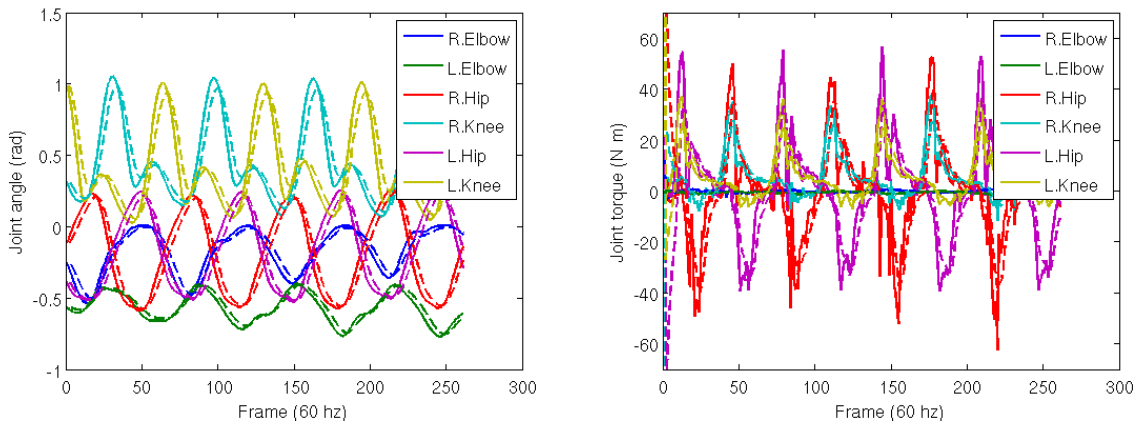

Fig 4. Trajectory reconstruction. Trajectories of selected degrees of freedom from the perturbation study. Solid lines show ground truth. Dashed lines show computed data. Simulated spring forces make the computed data lag behind and smooth the ground truth.

Test3: Whole body reaching

The previous demonstrations report on tests of the accuracy of the system in completely artificial situations. Herein we describe three tests of the whole body model's ability to fit data obtained from human subjects. The first test focuses on ground force and shows the result of estimates from the model compared to an independent ground force measure. The first test uses from a subject carrying out successively more difficult reaches in a virtual reality environment to test whether the models estimate of movement costs correlate with increasing task difficulty. The second test simulates data from an issue facing movements in an aging population. Do aging subjects' reduced use of arm swing while walking incur a movement cost, and does the HDM's estimate correspond to laboratory treadmill data? The final test demonstrates an important property of the model with respect to its degrees of freedom. The critical observation is that the degres of freedom of the model are constrained by virtues of their interconnections; thus, the control of a posture can be achieved with a very reduced set of key marker positions. This has implications for movement control programs.

The movement accuracy test are encouraging, but the importance of the method depends on its usefulness to capture the energetic cost of whole-body movements in a complex experimental setting. One such venue is a three-dimensional Virtual Reality (VR) environment. The advantage of the VR environment for studying human movements is that the dimensions and the dynamic variations of the parametric quantities describing setting can be varied with full experimental control.

In this particular experiment, we studied where human subjects needed to use whole-body movements cost choosing actions. From a particular start, a human subject touched targets suspended in 3D space. The experimental setup is demonstrated in Fig. 6. The subject is wearing the PhaseSpace suit and the nVisor head-mounted stereo display. From a fixed starting position, a subject is instructed to touch one of the targets and return to the starting position.

Tests were able to establish that, just focusing on integrated net torque and avoiding stiffness, the total cost of a movement recorded by our system reliably discriminates the energetic costs of the movement in the way hypothesized. The hypothesized cost of reaching for and touching

bioRxiv preprint doi: https://doi.org/10.1101/2020.08.23.262048; this version posted August 24, 2020. The copyright holder for this preprint (which was not certified by peer review) is the author/funder, who has granted bioRxiv a license to display the preprint in perpetuity. It is made available under aCC-BY-NC-ND 4.0 International license.

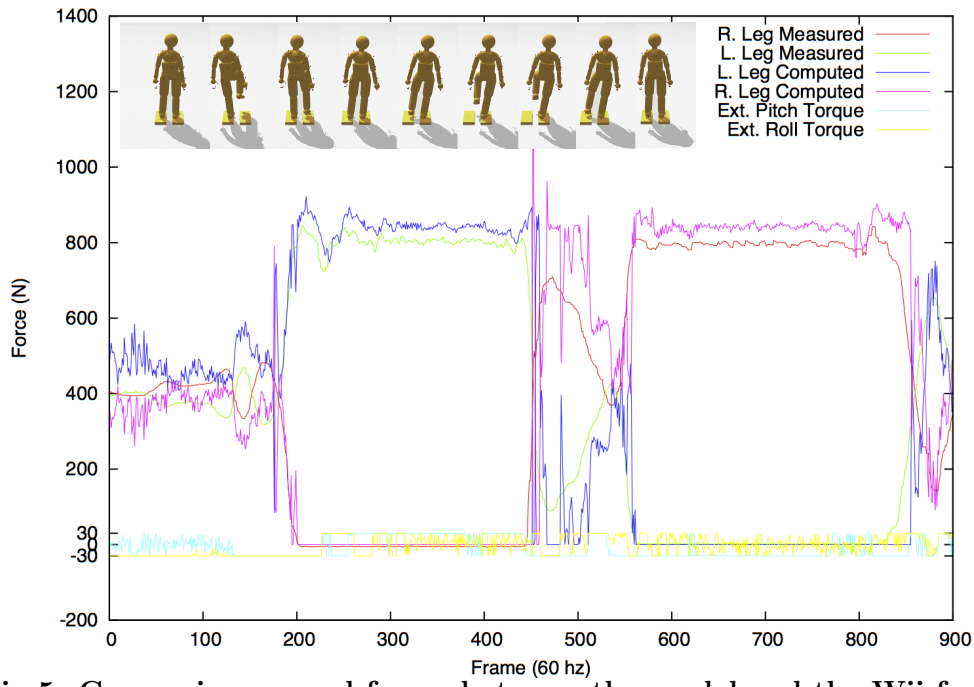

Fig 5. Comparing ground forces between the model and the Wii force plate. (Top) Two Wii force plates serve as accurate calibration reference. A subject stood on the two plates and then changed stances, balancing first on the left foot and next on the right. (Bottom) The comparison between the measurement systems is surprisingly good, during the stance phases, showing only a 10% difference between the *measured* ground forces and the *computed* forces.

each of the the targets was ranked on the basis of distance and height relative to the subject. Note that target #2 is the least expensive as the subject does not have to crouch or extend significantly to touch it. Targets 5 through 8 are more costly that targets 1 through 4 as they require that the subject take a step to touch them. These results were expected, but the point was to show that the overall setting and model could produce reliable torque estimates.

This demonstration shows that the model can be used in any setting where the cost of a movement is hypothesized to be a constituent factor. We develop this technique further in the next demonstration.

Test4: Comparing the HDM with a prior experimental result

Once the stiffness parameters were adjusted appropriately, can it reproduce the results of a stiffness modulating experiment? The experiment we tried was to replicate is that of Ortega el al. [63]. They showed that arresting the arm swing during treadmill walking incurred an increased metabolic cost of 6%. Our hypothesis was that to reproduce this result we could modify our walking data for the model so that the arms were clamped by the sides with stiff stationary markers.

To test this feasibility, we used one of our HDM walking data sets in a test situation. The cost of walking was computed and with a modification designed to model the data in [63]. To simulate their experiment, we modified the model data so the arms could swing with the walking gait for the standard case, but for the restricted case, the arms were constrained by markers that move with the stride but are not allowed to swing. Since the arms were not allowed to

bioRxiv preprint doi: https://doi.org/10.1101/2020.08.23.262048; this version posted August 24, 2020. The copyright holder for this preprint (which was not certified by peer review) is the author/funder, who has granted bioRxiv a license to display the preprint in perpetuity. It is made available under aCC-BY-NC-ND 4.0 International license.

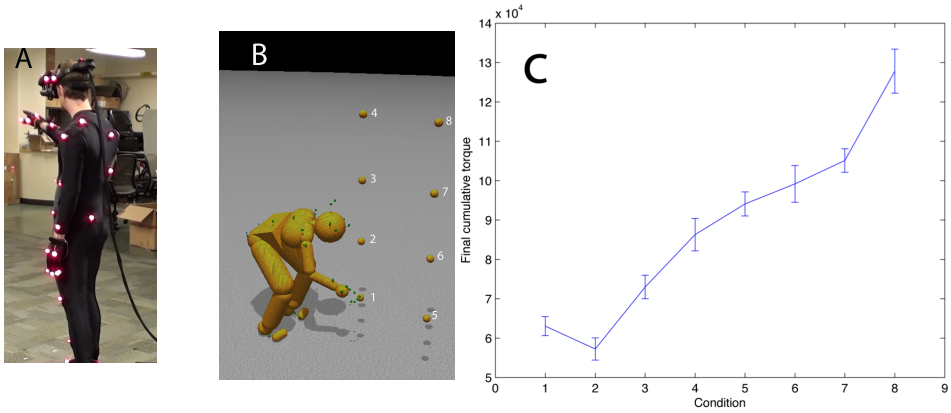

Fig 6. Reaching in Virtual Reality A) A subject reaches to touch virtual targets seen in a HMD. The Ss' reach is unconstrained. B) The subject reaches to the different numbered targets on separate trials. C) The average integrated torque over 10 trials per reach shows that the method reliably discriminates between movement costs for the further and higher locations.

balance the leg movements, we expected the energetic cost to be higher. As shown in Figure 7, the result was that the constrained walk was about 6 % more expensive than the standard walk, which was essentially the value obtained by the Farley lab. The use of the HDM in imitating this experiment shows off the utility of the model; no elaborate tuning was necessary to obtain the preliminary result other than restraining the arms.

test 5: Controlling poses with reduced degrees of freedom

Tests of movement accuracy revealed that the dynamics engine was able to tolerate significant noise levels added to the marker positions and still produce reasonable walking gaits. However, another possibility is to do away with many of the markers altogether and use a subset to constrain the dynamics. This property could have been expected from studies of muscle synergies, which show that muscle contractions coordinate in movement generation [25, 26].

Tests show that for many movements, with suitable internal stiffness, it is only necessary to control the location of a reduced set consisting of the head, hands, and feet markers. Fig. 8 shows a qualitative comparison between a pose found using the whole marker set (on the left) and one found using only head, hands, and feet(on the right). To achieve the reduced marker pose, we started the model in an upright stance with the arms by the side, and then the reduced set markers are moved slowly along trajectories that leave them in the final posture. The straight arms take advantage of the elbow joint angle limitation. Joint limits on the knees and elbows and general joint stiffness naturally bias the physics engine to find a pose that is very close to the fully constrained pose. Body inertia and joint stiffness naturally clean up minor noise and occlusions in the captured marker data. The resulting joint angles in transit allow the specification of the complete set of dynamic torques.

This result has important general implications. First off, the finding suggests that the kinematic plan for movements can be compressed into a subset of formative trajectories, leaving the remaining degrees of freedom interpolated using the body's dynamic constraint.

Another aspect of this observation is that the reduced set can be used to adjust movements to individual circumstances, again leaving the detailed interpolation to the dynamics.

bioRxiv preprint doi: https://doi.org/10.1101/2020.08.23.262048; this version posted August 24, 2020. The copyright holder for this preprint (which was not certified by peer review) is the author/funder, who has granted bioRxiv a license to display the preprint in perpetuity. It is made available under aCC-BY-NC-ND 4.0 International license.

(a) walking with arm swing (left) and stiff arm (right).

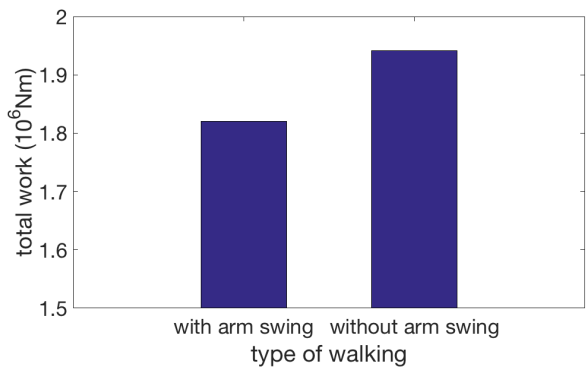

(b) energy cost

Fig 7. In a preliminary test of our design, the energetic cost of normal walking is compared to the case where the arms are constrained from swinging. Our hypothesis is that if subjects are instructed to walk without moving their arms, they will accomplish this by using co-contraction, and that this effect can be realized in the HDM with stationary markers that keep the arms vertical. The markers use joint stiffness values that are large enough to prohibit significant motion. As shown by the figure, the increased cost measured by the HDM is 6.1 %, extremely close to the the 6 % result obtained by Ortega.

Discussion

The paper has aimed to publicize the availability of a system for quantitatively modeling whole-body movements. Its 48 degrees of freedom allow models of scale that are robust to disturbances. In addition to being an analytical tool, it can also generate movements from a kinematic plan.

A central feature of the system is the production of the movements' energetic cost to provide the capability to compare different movement scenarios. Achieving this aim is notoriously tricky, owing to the lack of systems that can provide independent cost measures. One possibility is the use of force plates, as shown in our experiment, to measure the change in the stance. Another option is to use the system to produce correlations with similar tests with human subjects. Our research with stiff-arm warm, which reproduced the energetic difference of 6 % is one such example. A basic question concerned with the system is whether it can recover the cost of a

bioRxiv preprint doi: https://doi.org/10.1101/2020.08.23.262048; this version posted August 24, 2020. The copyright holder for this preprint (which was not certified by peer review) is the author/funder, who has granted bioRxiv a license to display the preprint in perpetuity. It is made available under aCC-BY-NC-ND 4.0 International license.

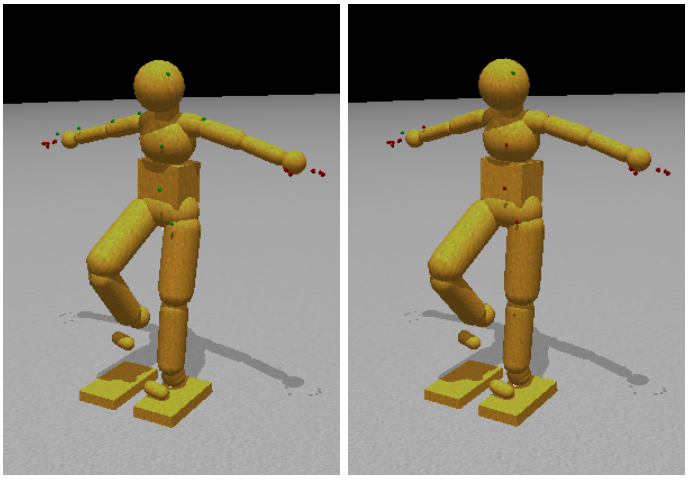

Fig 8. Movement control using dynamic synergies (a)Body configuration using all marker constraints.Note the similarity to the sparsely constrained pose. (b) Body configuration using constraints on only the head, hands, and feet. In many cases, the pose found using a full set of marker constraints is quite close to that found by a sparse set of constraints. These two images show almost no differences between using a full or a sparse set of marker constraints.

known physical system's complex motion, and this has been done, showing very high levels of accuracy. Once we have vetted the system in many such areas, it can be used as a predictive tool, as in the experiment showing the different costs of reaching to targets.

In addition, pf its use of a mechanism for interpreting experiments, the system can also serve as a useful base of theorizing about the human system's organization concerning its space-time performance since many of these issues are open. While an enormous amount of research in human motor control has produced ever more refined elucidations of subsystem components, a comprehensive theory at the level of large scale dynamics is still unsettled. One main obstacle is a description of how the motor cortex can communicate control information to drive the high temporal bandwidths of the spinal cord circuitry. Several possibilities were debated at the *Neural Control of Movement* conference in 2013 without definitive result, but the prospect that we have emphasized is that the motor cortex communicates a coded kinematic plan together with stiffness settings. A study with kinematics coded with temporal basis functions has shown that a kinematic plan can be coded to reduce the bandwidth needed by a factor of approximately 10^3 [27–29]. The HDM shows that such a model can play a useful role in studying the kinematic-plan model's consequences. In particular, the reduced degree of freedom control demonstration supports the *uncontrolled manifold* view wherein a subset of crucial degrees of freedom can direct a movement with the uncontrolled degrees of freedom interpolating the movement using the system's dynamics [30, 31]

The human dynamic model is relatively large, having 48 degrees of freedom. Additionally, its multiple DOF joints were designed to approximate human motion. The most important insight was the use of reduced degrees of freedom constraints in computing the dynamics. If the limitations are near the number of DOFs of the system, then the torque recovery can quickly become numerically unstable. However, up to 41 markers in the HDM provide sufficient constraints to integrate the dynamic equations reliably by allowing the natural dynamics of the system to interpolate the motion appropriately. One way of illustrating the robustness of the method is to combine a kinematic data set from the source with another set of dynamic

bioRxiv preprint doi: https://doi.org/10.1101/2020.08.23.262048; this version posted August 24, 2020. The copyright holder for this preprint (which was not certified by peer review) is the author/funder, who has granted bioRxiv a license to display the preprint in perpetuity. It is made available under aCC-BY-NC-ND 4.0 International license.

parameters. In tests, the data gathered with a different motion capture device is combined with the inertial data from another model to make a composite. This test used the Carnegie Mellon University's graphics laboratory's motion capture database. This beneficial and extensive database contains whole-body motion datasets for different human subjects performing a variety of natural motions. The database was created by motion capture and the positions of markers on the bodies are one of the primary sources of motion data. We did not know the individual dynamic parameters, but by adopting the database's marker conventions, we were able to use our dynamics calculation to compute joint torques for the composite system. Although the estimate is thus done for a synthetic pairing of kinematic data and dynamic parameters, the point is to show that, even with this combination, the integration is stable and leads to identifiable torques.

There are a number of ways to improve the system, but three are the most important. One limitation of our method for computing torque is that it is insensitive to muscle stiffness, which is both passive and can be actively modulated [32, 33]. Increasing stiffness will increase the overall net movement energetic cost and needs to be taken into account. The observation somewhat ameliorates this issue that in most natural tasks, subjects will try to minimize energetic costs and thus exploit natural dynamics whenever they can [34–36], reducing high levels of co-contraction. However, the ubiquitous use of spring as constraints means opening up the possibility that one can add springs to the joint degrees of freedom to model stiffness. These could also have parametric programmable spring constants to model muscle co-contraction. The second feature that could be added is a system to keep the human model upright. Any of the three human sources of this needed information - visual, vestibular, and proprioception - would be candidates for this practical constraint. The HDM at present uses a faux system of rotational torques at the center of gravity, but these could easily be replaced with more appropriate ankle torques. The third feature to be added is the separation of gravitational torques from control torques as only the latter effect metabolic cost directly. This improvement is a matter of modifying ODE's low-level code, and the plan is that this will be tackled in the near future.

The method has several advantages over alternate methods. First, it can be easily implemented in a single robust framework of the physics engine. Using the physics engine for multiple tasks allows a unique human model to be used from start to finish, rather than being forced to use the conventions built into a commercial package. Second, the method is fast. The simulation engine is designed for performance, making it possible to analyze movement in real-time and create interactive experiments with stimuli dependent on the feedback results. Third, the software is free. Freely accessible code, such as ODE, is useful because it facilitates comparison and collaboration in research.

In summary, the system's capability is a very stable set of integration equations that readily handle the inclusion of multiple points of surface contact. The HDM uses a closed loop step at each time step, so that the computed torques are appropriate for the new posture. In contrast, when the computed torques are saved and replayed, small errors in the kinematics build up, so that each set of torques is no longer appropriate for the computed posture and the overall system rapidly becomes unstable. The significance of these results extends beyond the simulation stability issue, and provides a strong argument for the suitability of the kinematic plan's close loop control as a biological model.

bioRxiv preprint doi: https://doi.org/10.1101/2020.08.23.262048; this version posted August 24, 2020. The copyright holder for this preprint (which was not certified by peer review) is the author/funder, who has granted bioRxiv a license to display the preprint in perpetuity. It is made available under aCC-BY-NC-ND 4.0 International license.

Materials and methods

The core of our simulations exploits the observation that realizations of constraints behave like implicit springs. The parameters that soften constraints into springs exhibit many advantageous properties. They stabilize the simulation, pushing a constrained system away from singularities, and reducing constraint error. Using the constraint solver as a joint controller makes it extremely easy to integrate inverse kinematics and inverse dynamics analysis into real-time applications that need physics computations for forward simulation. The solution is robust, fast, free, and allows one to work with a single general-purpose human movement model.

The integration requires an initial input of marker-based motion capture of the position of the markers over time. A PhaseSpace system creates these points from locations of optical markers attached to clothing or skin. Given this data, the human's pose, the relative position, and orientation of their body parts in space is determined by fitting a model to the optical marker data.

The central dynamics integration step combines the physics engine with a gradient-based learning approach to determine where captured markers sit on the different body parts of a character and where body parts attach to each other. This information allows the calculation of the model pose (or joint angles) over time by constraining a physically simulated model to satisfy marker constraints, joint constraints, and other relevant constraints such as non-penetration with the ground. Once provided with a sequence of poses, it is straightforward to constrain the model to transition through the pose sequence using internal joint torques.

Inverse Dynamics

The pose interface with markers provides the necessary initialization to calculate how much effort is required to accomplish a particular movement. For the human model, this amounts to knowing the torques to apply at each joint. The formulation can correctly compute the desired force measurements given the constraints, such as the angular velocity of each joint, with minimal effort. The process is straightforward. Given the current joint angle and the desired joint angle for the next frame, the relative angular velocity of the body parts is constrained as to achieve the target orientation on the next frame. Contact constraints are necessary to prevent ground surface penetration. The ODE physics library handles the constraints and solves the torques and forces that are used to satisfy each constraint in the process.

For computing inverse dynamics, the first step is to initialize the model to a starting dynamic state. The initial state can be found from two consecutive frames of kinematic pose data. The model pose is set by using the second frame of data, and the initial linear and angular velocity of each joint is computed by taking the finite difference between the two frames (and dividing by the timestep). Computing velocity through finite differences is appropriate for a physics engine using first-order semi-implicit Euler integration.

The next step is to find the torques between the second and third frames of pose data by using the finite difference between poses to compute angular velocities that will move the model from the second to third pose. Differentiating again, this time between the current and future velocity gives a target acceleration that becomes a constraint on the model. The primary difference between this step and the previously discussed method for finding pose from marker data is that there are no marker constraints dragging the body into place, and the internal muscle stiffness drives the model toward a target pose on each frame instead of toward a 'default' pose. Because there are fewer constraints in play, stiffer muscle forces are used, but the absolute forces the

bioRxiv preprint doi: https://doi.org/10.1101/2020.08.23.262048; this version posted August 24, 2020. The copyright holder for this preprint (which was not certified by peer review) is the author/funder, who has granted bioRxiv a license to display the preprint in perpetuity. It is made available under aCC-BY-NC-ND 4.0 International license.

muscles can apply are limited to prevent muscle forces from being unreasonably large.

The overall idea behind the method for calculating joint torques is straightforward and has been implemented in Open Dynamic Engine. The mathematics underlying the rigid body simulation software used in our work is explained in the Appendix section.

Human Model

Our techniques use a simulated model of the human whose movement is analyzed. The first order of business is to build a physical model capable of representing human movements. The accuracy of the model influences the outcome of the analysis. The humanoid model is a collection of rigid bodies connected by joint constraints. We present here a method for using marker data to help determine the dimensions of the model segments and where markers attach to the model to a human subject.

The technique for fitting a model to data begins with a character model that serves as a template, Fig. 9, providing the number of body segments and topology of the model. We further require that labeled markers used in motion capture be assigned to specific model segments. It may be straightforward to derive these using a technique such as in [16, 17]. However, it is also not difficult to do by hand. It would become tedious if one had to go through the process for many different models. Fortunately, the motion capture suit typically puts the markers on the same body segments, even if they are in slightly different places, and the body segments have different dimensions.

The model consists of n_b rigid bodies connected by n_j joints. In this case, each joint consists of three to five constraints. Each joint connects two rigid bodies with anchor points (center of rotation) defined in the reference frame of both bodies. The joint constraints keep the anchor points relative to the two bodies together in the global frame. If bodies b_j and b_k are connected, a joint constrains them together at a common point. The joint anchor relative to body b_j is $\tilde{\boldsymbol{c}}_{jk}$. The anchor for body b_k is $\tilde{\boldsymbol{c}}_{kj}$. The joint constraint drives these points together in the global frame, creating three constraint rows:

$$\boldsymbol{\phi}_{jk} = \boldsymbol{R}_j \tilde{\boldsymbol{c}}_{jk} + \boldsymbol{x}_j - \boldsymbol{R}_k \tilde{\boldsymbol{c}}_{kj} + \boldsymbol{x}_k$$

The locations of these anchor points determine the segment dimensions (bone lengths) of the character model.

Markers, each assigned to a specific rigid segment, represent a point on the human body. We seek anchor points that allow markers to remain approximately stationary relative to their assigned body segment. It is generally impossible to precisely find such a configuration (without creating an unreasonable number of body segments) because of soft-tissue artifacts (STAs). Skin and joints are not rigid. They stretch and give as muscles pull the bones. Modeling the body in maximal coordinates provides a way to model STAs explicitly.

Given a pre-defined model topology and markers assigned to specific model segments, we seek to find the joint anchor points between segments and the marker attachment points relative to the model segments. If the ith marker is assigned to the jth rigid body ($\boldsymbol{p}_i \rightarrow b_j$) at relative point $\tilde{\boldsymbol{s}}_{ij}$, we model the marker's attachment as a three dof constraint:

$$\boldsymbol{\phi}_{ij} = \boldsymbol{p}_i - \boldsymbol{R}_j \tilde{\boldsymbol{s}}_{ij} - \boldsymbol{x}_j$$

The process models markers from an arbitrary point in time as infinite point masses. As bodies of infinite mass, constraint forces do not affect the markers' trajectories but only the bodies

bioRxiv preprint doi: https://doi.org/10.1101/2020.08.23.262048; this version posted August 24, 2020. The copyright holder for this preprint (which was not certified by peer review) is the author/funder, who has granted bioRxiv a license to display the preprint in perpetuity. It is made available under aCC-BY-NC-ND 4.0 International license.

they are anchored to. Initially, markers are anchored at $\tilde{\boldsymbol{s}}_{ij} = \begin{bmatrix} 0 \\ 0 \\ 0 \end{bmatrix}$. This mapping attaches the marker to body b_j's center of mass.

This mapping is a very rough estimate of the marker attachment points on the model segments, but it is sufficient because of the flexible nature of constraints in the simulation software. Setting the *CFM* parameter of the marker constraints to $\beta = 10^{-3}$ and setting the model joint constraint *CFM* to $\beta = 10^{-5}$ makes the body segments hold together tightly, while still allowing the markers to pull the body into shape. Several timesteps of simulation allow the model to relax to a fixed pose. We then take the markers in their current configuration and reattach them to their respective segments. Relaxing the marker attachments this way improves the fit for this particular frame of marker data. Iteratively repeating this process with multiple frames of marker data, we therafter update the marker attachment points by some learning rate, η_m: $\tilde{\boldsymbol{s}}'_{ij} = (1-\eta_m)\tilde{\boldsymbol{s}}_{ij} + \eta_m \boldsymbol{R}_j^{\mathrm{T}} (\boldsymbol{p}_i - \boldsymbol{x}_j)$. Gradually updating attachment points, using different frames of data, effectively descends the error gradient of the marker positions relative to the body:

$$\min_{\tilde{\boldsymbol{s}}} \sum_{t=1}^{T} \sum_{i=1}^{n_m} \|\boldsymbol{p}_i - \boldsymbol{R}_j \tilde{\boldsymbol{s}}_{ij} - \boldsymbol{x}_j\|$$

The decrease in marker error affected by model dimension error. Conveniently, joint anchor constraints behave the same as the marker attachment constraints. With an arbitrary frame of marker data and using a marker *CFM* of $\beta = 10^{-4}$, if the markers constraints cannot be satisfied, they will pull the joint anchors apart slightly. For each joint we find a new common anchor point in the global frame by taking the average between the two unsatisfied anchor points that the joint constraint is trying to pull together. We then move the anchor points toward that point according to learning rate η_l:

$$\tilde{\boldsymbol{c}}'_{jk} = (1-\eta_l)\tilde{\boldsymbol{c}}_{jk} + \eta_l \boldsymbol{R}_j^{\mathrm{T}} (\boldsymbol{R}_k \tilde{c}_{kj} + \boldsymbol{x}_k - \boldsymbol{x}_j)$$

For any frame, errors will cause the markers to stretch from their attachment points and joint anchor points to stretch apart from each other. Both marker attachment points and the joint anchors can be updated simultaneously to decrease the error for that frame. However, the local solution that perfectly satisfies one frame may make another frame worse. This step presents an evident gradient descent approach to finding the joint anchors and marker attachments: using several frames, compute an average adjustment to the marker attachments, and joint anchors that reduce the error. Make the adjustment to both anchors and attachments and then iterate. It may be advisable to employ the standard machine learning practice of a validation set to ensure that the error continues to decrease and avoid overfitting. This technique relies on spring-like constraints made possible in maximal coordinates.

Although this method could easily be automated, in practice, the research did not rely on very many different models and so the system uses a mechanism for relaxing the marker attachment points and joint anchors with the click of a button in the graphical user interface (Fig. 1). With a new data set, a handful of iterations proved sufficient to produce a reasonable model with marker attachments that fit the data well enough for further analysis. This algorithm does not address joint limits on a range of motion. These can also be learned [48], but in our case, the range of motion for each joint is set *a priori*. After determining segment lengths, we set other segment dimensions as appropriate to fit against the markers. Mass properties for each segment assume uniform density by volume.

bioRxiv preprint doi: https://doi.org/10.1101/2020.08.23.262048; this version posted August 24, 2020. The copyright holder for this preprint (which was not certified by peer review) is the author/funder, who has granted bioRxiv a license to display the preprint in perpetuity. It is made available under aCC-BY-NC-ND 4.0 International license.

Model Segments

Having addressed the issues in attaching the model to motion capture data, we turn to the construction of the physical model capable of representing human movements. Fig. 9 shows the number of body segments and topology of the model. The humanoid model is a collection of rigid bodies connected by joint. Each joint connects two rigid bodies with anchor points (center of rotation) defined in the reference frame of both bodies. The locations of these anchor points determine the segment dimensions (bone lengths) of the character model.

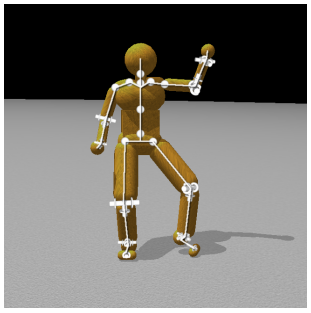

B

Joint	Part 1	Part 2	DOF/joint	Total DOF
Cervical	Head	Neck	3	3
Thoracic	Neck	Upper Torso	3	3
Lumbar	Upper Torso	Lower Torso	3	3
Sacral	Lower Torso	Pelvis	3	3
c.Clavicle	Upper Torso	c.Collar	3	6
c.Shoulder	c.Collar	c.Upper Arm	3	6
c.Elbow	c.Upper Arm	c.Lower Arm	2	4
c.Wrist	c.Lower Arm	c.Hand	2	4
c.Hip	c.Pelvis	c.Upper.Leg	3	6
c.Knee	c.Upper Leg	c.Lower Leg	2	4
c.Ankle	c.Lower Leg	c.Heel	2	4
c.Tarsal	c.Heel	c.Sesamoid	1	2

Fig 9. The 48 internal DOFModel A. Four ball-and-socket joints connect five body-segments along the spine from the head to the waist. Ball-and-socket joints are also used at the collar-bone, shoulder, and hip. B. A summary of the joints used in the model. c. = chiral: there are two of each of these joints (left and right). Universal joints are used at the elbows, wrists, knees, and ankles. Hinge joints connect the toes to the heels. All joints limit the range of motion to angles plausible for human movement. Our model assumes that joint DOFs summarize the effects of component muscles.

Labeled markers are assigned to specific model segments. It may be straightforward to derive these using a technique such as in [16, 17]. However, it is also not difficult to do by hand, as shown in Fig 10. The motion capture suit typically puts the markers on the same body segments, even if they are in slightly different places and the body segments have different dimensions.

Given this pre-defined model topology and markers assigned to specific model segments, the next step is to find the joint anchor points between segments and the marker attachment points relative to the model segments. Markers, each assigned to a specific rigid segment, represent a point on the human's body. Anchor points should allow markers to remain approximately stationary relative to their assigned body segment. It is generally impossible to find such a configuration exactly (without creating an unreasonable number of body segments) because of soft-tissue artifacts (STAs), that are present because skin and joints are not actually rigid; they stretch and give as muscles pull the bones. Modeling the body in maximal coordinates provides a way to model STAs explicitly, as discussed.

Model degree of freedom details The model structure consists of 21 separate rigid bodies connected by 20 joints (Fig 9). The relative orientation of some bodies is constrained by using universal joints for the elbows, wrists, knees, and ankles and hinge joints to connect the toes to

bioRxiv preprint doi: https://doi.org/10.1101/2020.08.23.262048; this version posted August 24, 2020. The copyright holder for this preprint (which was not certified by peer review) is the author/funder, who has granted bioRxiv a license to display the preprint in perpetuity. It is made available under aCC-BY-NC-ND 4.0 International license.

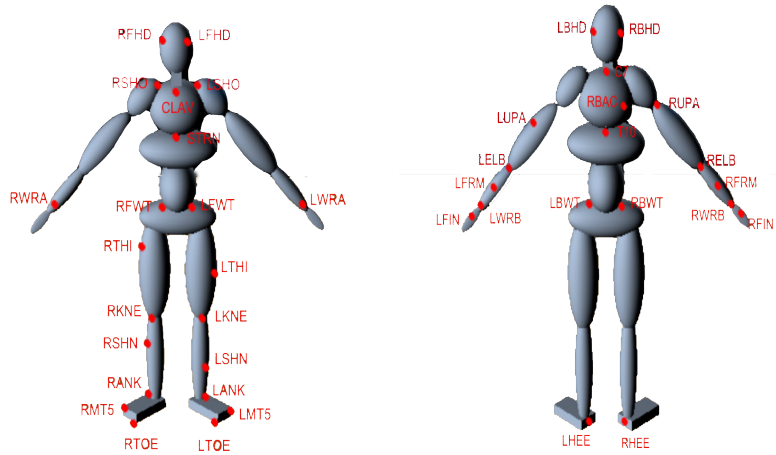

Fig 10. Marker arrangement on the motion capture suit. The suit contains 51 markers as shown by the LEDs in total but only 41 are used in the model e.g. Markers that are used are present on the fingers. Markers can easily assigned to specific model segments. For example, the markers of RBHD, RFHD, LFHD and LBHD are assigned to Head segment while the markers of RBWT, RFWT, LFWT and LBWT belong to Pelvis segment.

the heels. Universal joints restrict one angular degree of freedom; e.g., when the arm is bent at the elbow, the forearm cannot rotate around the principal axis of the upper arm unless the upper arm itself rotates. However, the forearm can rotate at the elbow around its own principal axis (modeling the twisting movement of the radius and ulnar bones). All other joints are left as ball-and-socket joints with three angular degrees of freedom: hips, shoulders, collar-bones, upper-neck, lower-neck, upper spine, and lower spine. This arrangement of joints leaves a total of 48 unconstrained internal degrees of freedom. An advantage of building humanoid model in this way is that joint connections are not treated as holonomic (perfectly rigid) constraints, but rather as very stiff springs that hold body parts together like tendons and muscles.

Given motion capture data of a subject, the model is fit to the subject's dimensions and joint-range-of-motion is constrained to approximate the subject's flexibility. Additionally, the model segments have inertial matrix properties. The initial mass assignment to each segment assumes a uniform density of water ($1000\frac{kg}{m^3}$) for the volume associated with each rigid body. The mass assignment should be modified to roughly match that of a specific subject. The increased fidelity, required for individual subjects in clinical biomechanics research would employ more sophisticated techniques for a better approximation of mass distribution in the model. Interestingly, however, the experimental results below show that even this low fidelity model is sufficient to produce high-quality data that compares favorably with data gathered from independent sensors.

Pose Fitting

Various commercial packages provide different methods for converting marker trajectories into sequences of body poses, but they can be time-consuming, expensive, or difficult to use. This section describes an approach related to [18] and [19] that is free, fast, uses intuitive parameters,

bioRxiv preprint doi: https://doi.org/10.1101/2020.08.23.262048; this version posted August 24, 2020. The copyright holder for this preprint (which was not certified by peer review) is the author/funder, who has granted bioRxiv a license to display the preprint in perpetuity. It is made available under aCC-BY-NC-ND 4.0 International license.

and allows the user to fit markers to whatever model they wish.

The method uses the physics engine to constrain a character model to fit marker data and other constraints. Markers are modelled as infinitely massed points attached to the character model. Given a frame of marker data, the position and orientation of all body segments can be found by balancing internal joint targets and external marker data. From the global position and orientation of the different body segments, it becomes a simple matter to compute relative orientations (joint angles).

The internal degrees of freedom are limited by range of motion constraints, e.g. the elbows and knees cannot bend backwards. All other joints have similar range-of-motion limitations based on the subject's flexibility. Furthermore, each joint is set to have a "target state", a preferred relative orientation between its connected bodies. These preferences can be thought of as "muscle stiffnesses" and are modeled as weak constraints with limited force. Joint limits and stiffness serve as a prior over possible poses so that in the absence of any marker data at all, the model still takes on a pose. Consequently, every internal degree of freedom is constrained to some degree.

These constraints hold the model together and give it a default pose. Marker data pull the model from the default pose into a new pose, e.g. Fig 11. For a given frame of motion capture data, each marker is connected to its associated body segment with a ball-and-socket joint constraint. A total of 41 markers, which do not contribute any degrees of freedom because of their infinite mass, attach to the character model, adding an additional $3 \times 41 = 123$ constraint dimensions.

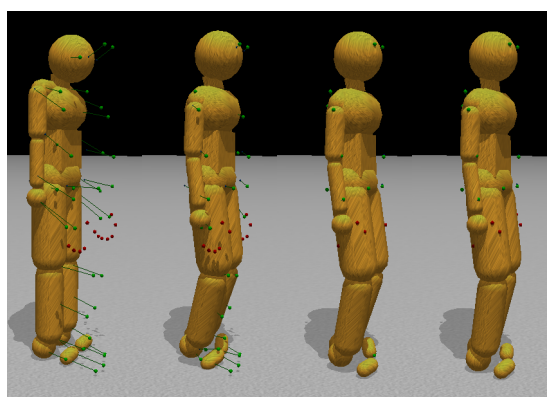

Fig 11. Pose fitting. Initially the motion capture data points are in a very different configuration than the initial stance of the model. To find the appropriate correspondences, simulated markers attach to the humanoid model through ball-and-socket joints and pull the body parts into place, subject to model joint constraints. The left to right sequence in the figure shows the body targets being gradually reconciled with the external markers.

Inverse dynamics

Vestibular system balance capability The torque calculation by the HDM is ideal in the sense of solving the dynamic equations, but in the actual situation there needs to be a corrective system for incidental errors. In the human system there are multiple corrective system based on vision, proprioception and the vestibular system. Such corrective systems have been extensively studied e.g. [20–22].

bioRxiv preprint doi: https://doi.org/10.1101/2020.08.23.262048; this version posted August 24, 2020. The copyright holder for this preprint (which was not certified by peer review) is the author/funder, who has granted bioRxiv a license to display the preprint in perpetuity. It is made available under aCC-BY-NC-ND 4.0 International license.

For the HDM, discrepancies between the model and human that created the data necessitate artificial "residual" forces to keep the model from falling over when dynamically reproducing most movements. A 6 degree of freedom joint between the waist segment and the global frame generate the external forces. A weak, limited spring constrains the waist segment to achieve its recorded pose relative to the global frame. The experiments show that attaching the external constraint to the head or the feet has little noticeable difference. The non-realistic external forces (residuals) account for noise as well as discrepancies between the model and the human generating the data. In particular, differences in how the feet interact with the ground cause errors in our analysis. In most cases it is only necessary to constrain two of the 6 angular degrees of freedom (pitch and roll), leaving the other four external degrees of freedom disabled. The two angular constraints keep the body from falling over but allow it to move about through simulated ground interactions.

The stabilization system completes the model. It can be implemented in parallel, with the control used to stabilize the residual necessary to balance. With this included, the simulation can reproduce highly dynamic motions, e.g. see Fig 2, which shows a jumping sequence made originally by a human subject and recreated using the torques used by the inverse dynamics model.

Finally, collisions between the ground and the feet also influence the model pose. Each foot can form up to three contact points with the ground. Inequality constraints at these points prevent penetration with the ground. When both feet are firmly on the ground, all markers are actively pulling the body into a pose, all joints are holding the body together, and joint limits and stiffness are biasing the relative orientation of the bodies. The experiments in next section show that the model can simulated the ground force correctly.

Supporting information

S1 Appendix. For each human subject we construct a dynamic model and force that model to follow the subject's motion capture data, which leads directly to the recovery of joint angles. Our algorithm constrains the dynamic model to track these angles and consequently can estimate the correct joint torques. This concept was originally demonstrated in two dimensions for human walking by [37]. We have extended the method to the significantly more demanding case of of 48 DOFs in three dimensions and arbitrary posture changes. Fig. 9 lists the body segments. The dimensions of each segment are matched those of an individual subject. The principal difficulty is that the constraints in the high DOF 3D model present many delicate numerical issues for the ODE solver that need to be addressed [14]. Currently the dynamic model does not attempt to model stiffness components, with the consequence that it can only directly recover the net torques at each DOF.

For data capture a subject wears the motion capture system developed by PhaseSpace. Each PhaseSpace LED marker is mapped to a corresponding point on the model. The markers are then introduced into the physics simulation as kinematic bodies without collision geometry. As a heuristic, each marker kinematic body is effectively treated as having infinite mass so that when another dynamic body is attached through a joint constraint to a marker, only the dynamic body's trajectory can be changed by the constraint.

The body segments are used by the simulation for both collision detection and the calculation of mass properties. Mass and inertial properties are computed from the volume of the body parts using a constant density of $1000\frac{Kg}{m^3}$. The dimensions and articulation are designed to

bioRxiv preprint doi: https://doi.org/10.1101/2020.08.23.262048; this version posted August 24, 2020. The copyright holder for this preprint (which was not certified by peer review) is the author/funder, who has granted bioRxiv a license to display the preprint in perpetuity. It is made available under aCC-BY-NC-ND 4.0 International license.

allow the model to reproduce most movements the human can make. For example, joints at the elbows have two DOFs to reproduce the hinge movement of the elbow as well as the twisting movement of the radius and ulna bones in the arm. Joint DOFs are also limited to prevent impossible movements such as reverse bending of the elbows or knees.

The PhaseSpace motion capture system records 41 3D positions of specific human body locations over time and maps these markers to appropriate locations on the model. When the simulation is stepped forward, a constraint solver attempts to find a body state that satisfies the internal joint constraints, the external marker constraints, and other constraints such as ground forces, joint stiffnesses, and conservation of momentum. Knowing the kinematics allows the recovery of the dynamics, since the joint velocities allow the equations of motion to be inverted. The retrieved forces can be used to generate feed-forward torque profiles for actuating the character.

When modeling human movements, however, we assume that the human body does not collide significantly with itself and so typically only process collisions between the model and the ground. Collisions between the model and the ground, however, play an important role in analyzing and synthesizing movement data such as walking. Collision handling involves creating a constraint between the colliding bodies and is the primary contribution of the model. We will describe this methodology after first introducing the physical simulation details.

Physical simulation involves a large number of different variables to represent constraints and relevant physical quantities. Table 1 presents specific symbols and their meanings for reference.

Scalars are represented with lower-case, un-bolded symbols: x. Bold lower-case symbols represent column vectors,

$$\boldsymbol{x} = \begin{bmatrix} x_1 \\ x_2 \end{bmatrix}$$

Bold, upper-case symbols to represent matrices:

$$\boldsymbol{X} = \begin{bmatrix} \boldsymbol{x}_1 & \boldsymbol{x}_2 \end{bmatrix} = \begin{bmatrix} x_{11} & x_{12} \\ x_{21} & x_{22} \end{bmatrix}$$

Dot-notation to indicates time derivative: $\dot{x} = \frac{dx}{dt}$. The circumflex accent indicates a 3d vector being used as a skew-symmetric matrix representing a cross-product operation:

$$\hat{\boldsymbol{x}}\boldsymbol{y} = \begin{bmatrix} 0 & -x_3 & x_2 \\ x_3 & 0 & -x_1 \\ -x_2 & x_1 & 0 \end{bmatrix} \begin{bmatrix} y_1 \\ y_2 \\ y_3 \end{bmatrix} = \boldsymbol{x} \times \boldsymbol{y}$$

Coordinates are typically relative to a global reference frame. However, a tilde, $\tilde{\boldsymbol{x}}$, indicates a quantity that uses a local reference frame, e.g., a body-relative frame, rather than the global frame. We use subscripts to indicate that a quantity refers to a specific dimension, a particular rigid body, a point in time, but clarify the subscript's meaning when necessary to remove ambiguity. Table 1 introduces the primary symbols within the text.

For conciseness in notation, we typically combine angular and linear quantities as a single symbol. This representation is used both for position and orientation even though orientation does not conveniently fit into a 3×1 vector. Fortunately, angular velocity and angular acceleration, $\boldsymbol{\omega}$and $\dot{\boldsymbol{\omega}}$, do combine well with linear velocity and acceleration $\dot{\boldsymbol{x}}$and $\ddot{\boldsymbol{x}}$, and it is these quantities that feature primarily when dealing with a constrained system. We will also represent the state of multiple bodies using a single symbol when convenient. For example, for a system with two

bioRxiv preprint doi: https://doi.org/10.1101/2020.08.23.262048; this version posted August 24, 2020. The copyright holder for this preprint (which was not certified by peer review) is the author/funder, who has granted bioRxiv a license to display the preprint in perpetuity. It is made available under aCC-BY-NC-ND 4.0 International license.

Symbol	Meaning
$\boldsymbol{x}$	position or state of one or more rigid bodies
$\dot{\boldsymbol{x}}$	velocity (usu. linear and angular)
$\ddot{\boldsymbol{x}}$	acceleration (usu. linear and angular)
$\boldsymbol{R}$	rotation matrix representing orientation of a body
$\boldsymbol{\omega}$	angular velocity
$\boldsymbol{q}$	quaternion representation of an orientation or rotation
m	mass of a single rigid body
$\boldsymbol{M}$	mass matrix
$\boldsymbol{I}$	identity matrix
$\boldsymbol{\mathcal{I}}$	moment of inertia tensor
n_b, n_c	number of bodies, number of constraints
$\boldsymbol{\alpha}, \boldsymbol{\beta}$	stabilizing parameters added to the equations of motion
$\phi()$	error or energy function for a single constraint
$\boldsymbol{J}$	matrix of partial derivatives of constraint error functions
h	timestep
$\boldsymbol{f}$	forces (and torques)
$\boldsymbol{\tau}$	torques
$\boldsymbol{\lambda}$	constraint forces

Table 1. Meanings of specific symbols used to discuss dynamic simulation

bodies, we will represent the combined linear and angular accelerations (a 12d vector) as $\ddot{\boldsymbol{x}}_t$. For this same 2-body system, Newton's law relating force, mass, and acceleration is as follows:

$$\begin{bmatrix} \boldsymbol{f}_{1t} \\ \boldsymbol{\tau}_{1t} \\ \boldsymbol{f}_{2t} \\ \boldsymbol{\tau}_{2t} \end{bmatrix} = \begin{bmatrix} m_1\boldsymbol{I} & \boldsymbol{0} & \boldsymbol{0} & \boldsymbol{0} \\ \boldsymbol{0} & \boldsymbol{\mathcal{I}}_{1t} & \boldsymbol{0} & \boldsymbol{0} \\ \boldsymbol{0} & \boldsymbol{0} & m_2\boldsymbol{I} & \boldsymbol{0} \\ \boldsymbol{0} & \boldsymbol{0} & \boldsymbol{0} & \boldsymbol{\mathcal{I}}_{2t} \end{bmatrix} \begin{bmatrix} \ddot{\boldsymbol{x}}_{1t} \\ \dot{\boldsymbol{\omega}}_{1t} \\ \ddot{\boldsymbol{x}}_{2t} \\ \dot{\boldsymbol{\omega}}_{2t} \end{bmatrix} \Rightarrow \boldsymbol{f}_t = \boldsymbol{M}_t\ddot{\boldsymbol{x}}_t$$

where $\boldsymbol{I}$ and $\boldsymbol{\mathcal{I}}_{it}$ are 3×3 block matrices.

Dynamic State Coordinates in the simulation world are defined relative to an arbitrary origin and basis set of directions. We refer to this inertial frame as the "global frame". Each rigid body also has its own point of reference and set of directions. Any point in the global frame can also be described relative to a body's frame of reference. It is convenient to define the point of reference of a body as its center of mass and use its principal inertial axes of symmetry as directions.

The position of the center of mass and orientation of a body within the global frame are here defined as $\boldsymbol{x}$ and $\boldsymbol{R}$ respectively. In 3d space, $\boldsymbol{x}$ is a 3×1 vector:

$$\boldsymbol{x} = \begin{bmatrix} x \\ y \\ z \end{bmatrix}$$

where x, y, and z are the distance from the origin along each of the three directions that establish the global frame of reference. For consistency, we deal with these distances in meters and assign

bioRxiv preprint doi: https://doi.org/10.1101/2020.08.23.262048; this version posted August 24, 2020. The copyright holder for this preprint (which was not certified by peer review) is the author/funder, who has granted bioRxiv a license to display the preprint in perpetuity. It is made available under aCC-BY-NC-ND 4.0 International license.

"up" to the positive z axis. The orientation $\boldsymbol{R}$ of a body is a 3×3 orthonormal matrix whose columns give the body's local direction frame relative to the global frame:

$$\boldsymbol{R} = \begin{bmatrix} r_{11} & r_{12} & r_{13} \\ r_{21} & r_{22} & r_{23} \\ r_{31} & r_{32} & r_{33} \end{bmatrix}$$

Conservation of momentum makes it necessary to keep track of the time derivative of these quantities: $\dot{\boldsymbol{x}}$ and $\dot{\boldsymbol{R}}$. Instead of explicitly representing $\dot{\boldsymbol{R}}$, it is convenient to keep track of the angular velocity:

$$\boldsymbol{\omega} = \begin{bmatrix} \omega_x \\ \omega_y \\ \omega_z \end{bmatrix}$$

The relationship between these quantities is

$$\dot{\boldsymbol{R}} = \hat{\boldsymbol{\omega}} \boldsymbol{R}$$

Representing orientation as a 3×3 matrix can be unwieldy. To properly represent an orientation (or pure rotation) it must be an orthonormal matrix. An orthonormal matrix uses nine elements to represent a property with only three degrees of freedom. Unfortunately, any three-element representation of orientation suffers from singularities [38]. We make use of unit-length quaternions to represent orientations and changes in orientation. Quaternions are convenient because of their close relationship to angular velocities. Quaternions are similar to an axis-angle representation of a rotation. A quaternion $\boldsymbol{q}$ represents a rotation by θ around unit vector $\boldsymbol{v}$ with four elements:

$$\boldsymbol{q} = \begin{bmatrix} q_w \\ q_x \\ q_y \\ q_z \end{bmatrix} = \begin{bmatrix} \cos\frac{\theta}{2} \\ v_x \sin\frac{\theta}{2} \\ v_y \sin\frac{\theta}{2} \\ v_z \sin\frac{\theta}{2} \end{bmatrix}$$

From an arbitrary angular velocity $\boldsymbol{\omega}$, we can make a quaternion that represents the change in rotation that would occur during a timestep of h. After finding the amount of rotation $\theta_t = h\|\boldsymbol{\omega}_t\|$, one might naively find a "rotation quaternion" by normalizing $\boldsymbol{\omega_t}$ and then re-scaling by $\sin\frac{\theta_t}{2}$ for a final quaternion: $\boldsymbol{q}_t = \begin{bmatrix} \cos\frac{\theta_t}{2} \\ \frac{\boldsymbol{\omega_t}}{\theta_t}\sin\frac{\theta_t}{2} \end{bmatrix}$. However, the normalization step becomes unstable as θ_t approaches zero. To avoid that instability, we use the "sinc" function where $\operatorname{sinc}\theta = \frac{\sin\theta}{\theta}$. The sinc function allows us to remove the discontinuity that would result from division by zero and adds numerical stability. When θ is small, $\operatorname{sinc}(\theta)$ can be approximated to within machine precision using the first two non-zero terms of its Taylor expansion (see [38]). The result is a discrete-time "rotation quaternion":

$$\boldsymbol{q}_t = \begin{bmatrix} \cos\frac{\theta_t}{2} \\ \frac{h}{2}\operatorname{sinc}\frac{\theta_t}{2}\boldsymbol{\omega_t} \end{bmatrix} \tag{1}$$

Given n_b bodies, the dynamic state of the ith body at time t is its position, orientation, linear velocity, and angular velocity: $\left\{ \boldsymbol{x}_{it} \quad \boldsymbol{R}_{it} \quad \dot{\boldsymbol{x}}_{it} \quad \boldsymbol{\omega}_{it} \right\}$. We will assume that all of these values are framed in the global coordinate system unless specified otherwise. The body dynamics are

bioRxiv preprint doi: https://doi.org/10.1101/2020.08.23.262048; this version posted August 24, 2020. The copyright holder for this preprint (which was not certified by peer review) is the author/funder, who has granted bioRxiv a license to display the preprint in perpetuity. It is made available under aCC-BY-NC-ND 4.0 International license.

also affected by the body's constant mass m_i and inertia tensor $\boldsymbol{\mathcal{I}}_{it}$. The moment of inertia tensor, $\boldsymbol{\mathcal{I}}$, is indexed by time because the body's orientation changes how the the mass is distributed relative to the world frame: $\boldsymbol{\mathcal{I}}_{it} = \boldsymbol{R}_{it}\tilde{\boldsymbol{\mathcal{I}}}_i\boldsymbol{R}_{it}^{\mathrm{T}}$. We assume that the inertia tensor is constant relative to the body-local frame of reference (i.e., bodies are rigid).

In simulation, the forces $\boldsymbol{f}$ applied to the rigid bodies come from three general sources. These are constraint forces ($\boldsymbol{f_c}$), gravitational and gyroscopic forces ($\boldsymbol{f_g}$), and user/control forces ($\boldsymbol{f_u}$): $\boldsymbol{f} = \boldsymbol{f_c} + \boldsymbol{f_g} + \boldsymbol{f_u}$.

Integration Step When a force is applied to a body, it translates into acceleration that is inversely proportional to the mass. Velocity is the time integral of acceleration, $\dot{\boldsymbol{x}}_t = \dot{\boldsymbol{x}}_{i0} + \int_0^t \boldsymbol{M}_i^{-1}\boldsymbol{f}_t dt$, and position is the time integral of velocity, $\boldsymbol{x}_{it} = \boldsymbol{x}_{i0} + \int_0^t \dot{\boldsymbol{x}}_{it} dt$. Because $\boldsymbol{f}_t$ may depend on $\boldsymbol{x}_t$ and $\dot{\boldsymbol{x}}_t$ as well as on discontinuous collisions and control inputs, analytic descriptions of body state are not usually possible. Instead we discretize the equations of motion and use a small, discrete timestep, h, to numerically approximate system dynamics. The most obvious thing to do is to linearize the force function, $\boldsymbol{f}_t$, and then take all the quantities from time t and use them to find the state at time $t + h$:

$$\dot{\boldsymbol{x}}_{t+h} = \dot{\boldsymbol{x}}_t + h\boldsymbol{M}^{-1}\boldsymbol{f}_t \tag{2}$$

$$\boldsymbol{x}_{t+h} = \boldsymbol{x}_t + h\dot{\boldsymbol{x}}_{t+h} \tag{3}$$

This "semi-implicit Euler" integration uses using the future velocity for computing position and is more stable than the standard formulation.

Although we lump orientation and position together as a single symbol, in practice there are a few distinctions that need mentioning. For example, gravity only applies to the linear state, while gyroscopic torques only apply to angular state. Gravitational forces are very straightforward, $\boldsymbol{f}_{\mathrm{grav}} = \boldsymbol{M}\boldsymbol{g}$, where $\boldsymbol{g}$ indicates the direction and magnitude of gravitational acceleration and is often very simple; e.g., for a single rigid body $\boldsymbol{g} = \begin{bmatrix}0 & 0 & -9.8 & 0 & 0 & 0\end{bmatrix}^{\mathrm{T}}$.

Rotation is a non-linear phenomenon. However, we can approximate the motion of a rotating body by adding torques that imitate gyroscopic effects, see [39]. Gyroscopic torques are applied to maintain conservation of angular momentum. Explicitly applying gyroscopic torques to bodies allows us to treat the rest of the system as though it conserved angular velocity rather than angular momentum. Thereafter, we can deal with the combined linear and angular quantities as a linear system.

The gyroscopic torques for each body are linearly approximated by

$$\boldsymbol{f}_{\mathrm{gyro}} = \begin{bmatrix}\boldsymbol{0} & \boldsymbol{0} \\ \boldsymbol{0} & \hat{\boldsymbol{\omega}}_t\end{bmatrix}\begin{bmatrix}\boldsymbol{0} & \boldsymbol{0} \\ \boldsymbol{0} & \boldsymbol{\mathcal{I}}_t\end{bmatrix}\begin{bmatrix}\boldsymbol{0} \\ \boldsymbol{\omega}_t\end{bmatrix}$$

These forces are zero if the three principal moments of the inertia tensor are equal. Otherwise, they represent the forces necessary for conservation of angular momentum. Unfortunately, this approximation tends to introduce energy into the system. We have reduced this problem in ODE by adding in additional terms as described in [39].

The constrained system is solved using mostly accelerations and velocities. At the end, however, it is necessary to integrate the velocities into new positions and orientations. Position and orientation are updated differently. For position, it is sufficient to multiply the linear velocity by the timestep and add it to the current position. Adding angular velocity to orientation is not

bioRxiv preprint doi: https://doi.org/10.1101/2020.08.23.262048; this version posted August 24, 2020. The copyright holder for this preprint (which was not certified by peer review) is the author/funder, who has granted bioRxiv a license to display the preprint in perpetuity. It is made available under aCC-BY-NC-ND 4.0 International license.

as straightforward. We integrate angular velocity into orientation by converting $\boldsymbol{\omega}_{i(t+h)}$ into a quaternion and then use the quaternion to rotate the current orientation forward in time following [38].

Constraint Equation When a rigid body is moving or spinning freely through space, the integration equations are sufficient to simulate dynamics. Adding constraints modifies the bodies' movements. Maintaining a relationship between two bodies requires forming a constraint on the state of the bodies. The integration equations tell us how to go from force to velocity and from there to position and orientation. To simulate an articulated model using maximal coordinates, we need to know what forces constraints apply to the bodies in the system.

To find the constraint forces, one must be able to mathematically describe the constraint. We define a multi-dimensional function over the combined position and orientation of all bodies in the system, $\boldsymbol{\phi}(\boldsymbol{x}_t)$, that produces a vector of size n_c specifying how much each constraint is violated, where n_c is the number of constraints acting on the system. For example, if the ith constraint keeps body b_2 a distance d above body b_1 in the z direction, we would have $\phi_i(\boldsymbol{x}) = x_{2z} - x_{1z} - d$. If b_2 is not separated from b_1 by a distance of d in the z direction, $\phi_i(\boldsymbol{x})$ reports the signed magnitude of that constraint error. For additional information on forming constraint equations, see [40, 41].

In general, the error for a constraint is non-zero. Given a measure of the error for a given state, we seek to find constraint forces, $\boldsymbol{f_c}$, that reduce the error over subsequent time steps [42]. Specifically, over the timestep h, we seek a force to reduce the magnitude of the constraint error by a fraction α. That is

$$\boldsymbol{\phi}(\boldsymbol{x}_{t+h}) = (I - \boldsymbol{\alpha})\boldsymbol{\phi}(\boldsymbol{x}_t) \tag{4}$$

where $\boldsymbol{\alpha}$ is a $k \times k$ diagonal matrix with each $\alpha_i \in [0, 1]$ representing the fraction of error reduction over a time step. In ODE, the α value is controlled through the *error reduction parameter* (ERP) which can be set independently for each constrained degree of freedom. In practice, it is not possible to remove constraint error completely ($\alpha = 1$) when using maximal coordinates because of error introduced by the various approximations employed to make the simulation linear and fast. Values of α typically fall within $[0.2, 0.8]$. Manipulating this value results in useful elastic and damping effects discussed later.

We use the symbol $\boldsymbol{J}_t$ to represent the $n_c \times 6n_b$ matrix of partial derivatives of $\boldsymbol{\phi}(\boldsymbol{x}_t)$. This matrix is a linear approximation of how the constraint error for each of the n_c constraints changes when the positions and orientations of the bodies change:

$$\boldsymbol{J}_t = \nabla\boldsymbol{\phi}(\boldsymbol{x}_t) = \begin{bmatrix} \frac{\partial\phi_1}{\partial x_{1t}} & \cdots & \frac{\partial\phi_1}{\partial x_{(6n_b)t}} \\ \vdots & \ddots & \vdots \\ \frac{\partial\phi_k}{\partial x_{1t}} & \cdots & \frac{\partial\phi_k}{\partial x_{(6n_b)t}} \end{bmatrix}$$

Finding the constraint forces that satisfy Eq. 4 involves removing all references to unknown future quantities. The Taylor expansion of $\boldsymbol{\phi}(\boldsymbol{x}_{t+h})$ at $\boldsymbol{x}_t$, truncated after the first order term, approximates the future constraint error:

$$(I - \boldsymbol{\alpha})\boldsymbol{\phi}(\boldsymbol{x}_t) = \boldsymbol{\phi}(\boldsymbol{x}_{t+h}) \approx \boldsymbol{\phi}(\boldsymbol{x}_t) + \boldsymbol{J}_t(\boldsymbol{x}_{t+h} - \boldsymbol{x}_t) \tag{5}$$

This truncation has the effect of treating all constraints as linear. Many constraints used to simulate various joints are linear; others, however, contain higher-order terms and this truncation is one potential source of error in simulation.

bioRxiv preprint doi: https://doi.org/10.1101/2020.08.23.262048; this version posted August 24, 2020. The copyright holder for this preprint (which was not certified by peer review) is the author/funder, who has granted bioRxiv a license to display the preprint in perpetuity. It is made available under aCC-BY-NC-ND 4.0 International license.

Combining the two integrator equations, Eqs. 2 and 3, gives the future position/orientation in terms of the present position, velocity, and forces:

$$\boldsymbol{x}_{t+h} = \boldsymbol{x}_t + h\dot{\boldsymbol{x}}_t + h^2\boldsymbol{M}_t^{-1}\left(\boldsymbol{f}_{ct} + \boldsymbol{f}_{gt} + \boldsymbol{f}_{ut}\right) \tag{6}$$

Equations 4, 5, and 6 combine to eliminate all references to future quantities:

$$(I - \boldsymbol{\alpha})\boldsymbol{\phi}(\boldsymbol{x}_t) = \boldsymbol{\phi}(\boldsymbol{x}_t) + \boldsymbol{J}_t\left(\boldsymbol{x}_t + h\dot{\boldsymbol{x}}_t + h^2\boldsymbol{M}_t^{-1}\left(\boldsymbol{f}_{ct} + \boldsymbol{f}_{gt} + \boldsymbol{f}_{ut}\right) - \boldsymbol{x}_t\right) \tag{7}$$

This leaves one unknown vector at time t: the constraint forces $\boldsymbol{f}_{ct}$. Rearranging and simplifying, we get

$$\boldsymbol{J}_t\boldsymbol{M}_t^{-1}\boldsymbol{f}_{ct} = -\frac{1}{h^2}\boldsymbol{\alpha}\boldsymbol{\phi}(\boldsymbol{x}_t) - \frac{1}{h}\boldsymbol{J}_t\dot{\boldsymbol{x}}_t - \boldsymbol{J}_t\boldsymbol{M}_t^{-1}\left(\boldsymbol{f}_{gt} + \boldsymbol{f}_{ut}\right) \tag{8}$$

Note that in rearranging the terms this way, we divided both sides by the squared timestep, h^2, effectively changing the problem from one dealing with positions to one dealing with accelerations. This conversion is possible because of the relationship established between acceleration and position by the semi-implicit Euler integrator.

Equation 8 is almost the equation that ODE solves when simulating physics. The right hand side is a desired acceleration. The first term on the right is the acceleration that would result in a velocity that would remove a fraction (α) of the constraint error. The second and third terms account for the effects of momentum (current velocity), gravity, and other forces (e.g., user control forces) applied to the bodies. Each constraint becomes its own dimension in a "constraint space". The Jacobian matrix $\boldsymbol{J}$ projects accelerations from global forces into constraint space.

In general, the matrix on the left hand side of Eq. 8 is not square, making the problem under-constrained (or in some cases, potentially over-constrained). However, we can use d'Alembert's principle [43] to restrict the constraint forces to lie in the constraint space.

Another method for arriving at the constraint equation is through the use of Lagrange multipliers. Consequently, the constraint-space forces are typically denoted with λ. The Jacobian transpose gives the relationship between a force applied in constraint space and force/torque applied in the full coordinate space: $\boldsymbol{f}_{ct} = \boldsymbol{J}_t^{\mathrm{T}}\boldsymbol{\lambda}_t$.

The vector, $\boldsymbol{\lambda}_t$, holds the generalized forces applied by each constraint on all the bodies involved in that constraint, whereas $\boldsymbol{f}_{ct}$ holds the sum of the constraint forces applied to each individual degree of freedom of each rigid body. The LHS of Eq. 8 can then be rewritten as $\boldsymbol{J}_t\boldsymbol{M}_t^{-1}\boldsymbol{J}_t^{\mathrm{T}}\boldsymbol{\lambda}_t$, where $\boldsymbol{J}_t\boldsymbol{M}_t^{-1}\boldsymbol{J}_t^{\mathrm{T}}$ is now a $n_c \times n_c$ positive semi-definite matrix.

Returning to maximal coordinates, we will compress Eq. 8 down to

$$\boldsymbol{J}\boldsymbol{M}^{-1}\boldsymbol{J}^{\mathrm{T}}\boldsymbol{\lambda} = \boldsymbol{w} \tag{9}$$

In general, the matrix $\boldsymbol{J}\boldsymbol{M}^{-1}\boldsymbol{J}^{\mathrm{T}}$ may be singular. It is very easy to end up with redundant or conflicting constraints. For example, a box resting on the ground may get a contact constraint at each corner. If each contact prevents interpenetration and sliding (i.e., applies friction) then the contacts constrain a total of 12 degrees of freedom on a single rigid body with only 6 degrees of freedom to be constrained. Conflicting or redundant constraints can break the solver if not dealt with beforehand. The means for dealing with the conflict is clever. The physics engine softens the constraint, allowing it to "slip" proportional to the amount of force necessary to maintain it.

bioRxiv preprint doi: https://doi.org/10.1101/2020.08.23.262048; this version posted August 24, 2020. The copyright holder for this preprint (which was not certified by peer review) is the author/funder, who has granted bioRxiv a license to display the preprint in perpetuity. It is made available under aCC-BY-NC-ND 4.0 International license.

Because mass is always positive, the force, λ, applied to a particular constraint and the resulting constraint-space acceleration will have the same sign. Softening the constraint is therefore a matter of subtracting a scaled copy of λ from the desired acceleration (the right hand side): $\boldsymbol{J}\boldsymbol{M}^{-1}\boldsymbol{J}^{\mathrm{T}}\boldsymbol{\lambda} = \boldsymbol{w} - \boldsymbol{\beta}\boldsymbol{\lambda}$, where $\boldsymbol{\beta}$ is an $n_c \times n_c$ diagonal matrix of (typically small) non-negative values. This subtraction, of course, is equivalent to adding $\boldsymbol{\beta}$ to the LHS. Adding these small values to the diagonal of the effective inverse-mass-matrix makes the constraints seem lighter to the solver and moves the matrix away from singularity:

$$\left(\boldsymbol{J}_t\boldsymbol{M}_t^{-1}\boldsymbol{J}_t^{\mathrm{T}} + \boldsymbol{\beta}\right)\boldsymbol{\lambda}_t = -\frac{1}{h^2}\boldsymbol{\alpha}\boldsymbol{\phi}(\boldsymbol{x}_t) - \frac{1}{h}\boldsymbol{J}_t\dot{\boldsymbol{x}}_t + \boldsymbol{J}_t\boldsymbol{M}_t^{-1}\left(\boldsymbol{f}_{gt} + \boldsymbol{f}_{ut}\right) \tag{10}$$

The original programmers built soft constraints into the ODE simulation code. The variable, β, tunable for each constraint, is known in ODE as the *constraint force mixing* parameter (CFM). At first glance, the addition of these parameters may seem loose and unprincipled. However, correctly setting the parameters, α and β, changes a hard constraint into a simulated implicit spring with first order integration (see [44]).

It is well-known that the formula for ideal damped spring force is identical to the formula for PD control. However, connecting these two facts, namely that (1) ODE's constraints are mathematically equivalent to implicit damped springs and (2) damped springs are equivalent to PD controllers, has not been exploited. This insight is key to the success of the methods presented here. Our derivation shows that ODE's constraints are, in fact, stable PD controllers along with examples of how to take advantage of this fact. We proceed by discussing proportional-derivative control and the mass-spring-damper equation.

Implicit Simulated Springs Proportional-derivative (PD) control is a common method used to compute forces that drive a system toward a target state. The PD control equation is the same as a mass-spring-damper system. There are two parameters, k_p and k_d, that determine what force should be applied to a degree of freedom at any point in time. The stiffness, also called proportional gain (k_p), specifies a force driving a degree of freedom toward its setpoint, $\bar{x}$ with strength proportional to the distance from the setpoint. The damping, also known as derivative gain (k_d), counteracts the current velocity, slowing the system down to avoid overshooting. When a system uses PD control to encourage a degree of freedom to move toward a target state, the control force f_{ut} at any instant in time is a function of the current position and velocity of the effective mass being controlled relative to its target:

$$f_{ut} = -k_p x_t - k_d \dot{x}_t \tag{11}$$

In a continuous time system, this controller is guaranteed to be stable as long as k_d and k_p are non-negative. With zero damping ($k_d = 0$) the system oscillates in a sinusoidal wave pattern whose frequency is determined by the stiffness and mass and whose magnitude is determined by the initial conditions. With zero stiffness and positive damping, the velocity of the system decays exponentially with higher damping converging to zero more steeply. Discrete sampling of these forces, however, ruins the stability conditions. The potential for instability is apparent if we consider a mass m that only experiences damping forces. Using the semi-implicit Euler integrator, Eq. 2, we plug in the damping forces from Eq. 11 to get

$$\dot{x}_{t+h} = \dot{x}_t - \frac{hk_d}{m}\dot{x}_t = \left(1 - \frac{hk_d}{m}\right)\dot{x}_t \tag{12}$$

bioRxiv preprint doi: https://doi.org/10.1101/2020.08.23.262048; this version posted August 24, 2020. The copyright holder for this preprint (which was not certified by peer review) is the author/funder, who has granted bioRxiv a license to display the preprint in perpetuity. It is made available under aCC-BY-NC-ND 4.0 International license.

Time (t), mass (m), and damping (k_d) should all be non-negative values. It is clear, then, from this equation, that if $\frac{hk_d}{m} > 2$, the velocity will oscillate between positive and negative values and grow in magnitude. This oscillation rapidly causes the simulation to "explode" and is annoyingly common when using PD control. Overly stiff springs hit a similar limit with explicit discrete integration that causes them to gain energy and explode. Consequently, explicit PD control gains are tricky to tune. They must fall within certain limits that depend on the timestep and the effective mass experienced by the system.

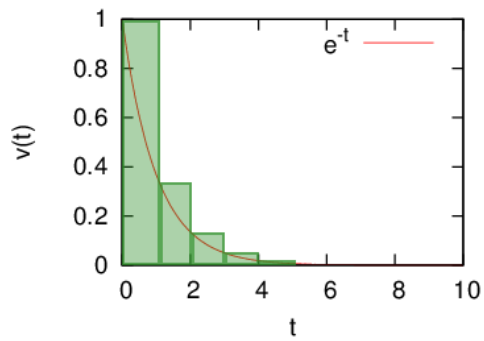

Fig 12. Explicit integration of damping forces is similar to the forward-method for approximating the area under a curve as a sum of rectangles. In this case it severely overestimates, leading to instability.

The cause for this instability lies in the discrete integration which is similar to approximating the area under a curve as the sum of multiple rectangles computed forward from the present (Fig. 12). One solution is to solve for the forces *implicitly*. Implicit integration is similar to approximating the area under a curve with fixed-width rectangles that end rather than begin on the curve. Rather than overestimate, this method tends to underestimate the area under an exponential curve. The resulting system does not explode, although it tends to dissipate rather than conserve energy. The implicit form of the damped-spring-law depends on the integrator it is applied to. Being 'implicit', in this case, specifies that spring forces are computed from the *future* state of the system. Consequently, Eq. 11 becomes the following, (note the changed temporal indices):

$$f_{ut} = -k_p x_{t+h} - k_d \dot{x}_{t+h} \tag{13}$$

We do not know the future position or velocity, but using the integrator equations, Eqs. 3 and 2, we reframe Eq. 13 in terms of the current quantities and then solve for f_{ut} to get

$$f_{ut} = -\frac{k_d \dot{x}_t + k_p x_t + hk_p \dot{x}_t}{1 + m^{-1}hk_d + m^{-1}h^2 k_p} \tag{14}$$

If we analyze a pure damped system as before but using Eq. 14, we end up with

$$\dot{x}_{t+h} = \dot{x}_t - \frac{hk_d \dot{x}_t}{m + hk_d} = \frac{m}{m + hk_d}\dot{x}_t$$

With k_d now in the denominator, even an infinite damping gain is stable, corresponding to the damping force that completely eliminates the current velocity in a single timestep. This stability allows us to make PD controllers with extremely stiff gains.

Stability is a nice property for a controller or simulator to have. We now show that the α and β terms added to the constraint equation change them into implicit springs. To see the

bioRxiv preprint doi: https://doi.org/10.1101/2020.08.23.262048; this version posted August 24, 2020. The copyright holder for this preprint (which was not certified by peer review) is the author/funder, who has granted bioRxiv a license to display the preprint in perpetuity. It is made available under aCC-BY-NC-ND 4.0 International license.

correspondence between Eq. 10 and Eq. 14, we consider a constraint that keeps a point mass at the origin along a single dimension: $\phi(x_t) = x_t$. The displacement function for this system has a trivial Jacobian: $J = 1$, meaning that $\lambda = f_c$. Assuming that external forces are zero, $f_g = f_u = 0$, Eq. 10 simplifies to

$$(m^{-1} + \beta) f_{ct} = -\frac{\alpha}{h^2} x_t - \frac{1}{h} \dot{x}_t \tag{15}$$

Assigning the α and β parameters[5] to be, $\alpha = \frac{hk_p}{hk_p + k_d}$ and $\beta = \frac{1}{h^2 k_p + hk_d}$, and isolating f_{ct}, Eq. 15 reduces to the implicit spring equation Eq: 14:

$$f_{ct} = -\frac{\left(\frac{hk_p}{hk_p+k_d}\right) x_t + h\dot{x}_t}{h^2 m^{-1} + h^2 \left(\frac{1}{h^2 k_p + hk_d}\right)} = -\frac{k_d \dot{x}_t + k_p x_t + hk_p \dot{x}_t}{1 + m^{-1} hk_d + m^{-1} h^2 k_p}$$

The consequence of this relationship is that every constraint in ODE can be thought of as an implicit spring. An important feature of this formulation is that the equations are solved simultaneously. When the implicit springs are solved simultaneously in the physics framework, the forces account for each other; without this change the system would be very fragile. Softening the constraints to springs makes it so that we can solve a system that would otherwise be over constrained. We can add more constraints than there are degrees of freedom.

Solving with Complementarity Conditions For simplicity, we compress Eq. 10 down to $\boldsymbol{A}\boldsymbol{\lambda} = \boldsymbol{w}$. When $\boldsymbol{A}$ is non-singular, we can solve for $\boldsymbol{\lambda}$ by inverting, or preferentially, using a fast, numerically-stable solver such as a Cholesky decomposition. Some constraints, however, come with additional conditions that need to be solved with extra machinery. In simulation literature, these are known as inequality constraints. For example, a contact constraint keeps two bodies from moving towards each other by defining an error function that is the separation of the contacting surfaces in the direction of one of the surface normals. If the surfaces are overlapping, then the error function has a negative value and a positive constraint force will accelerate the surfaces apart. This acceleration is as it should be. However, the linear system also applies forces to correct positive error; so the same constraint would also prevent the surfaces from separating.

The solution to this problem is to limit the amount of force available for satisfying the constraint. A contact constraint, in particular, limits the force to be non-negative. Contact friction constraints are limited on both sides to be proportional to the contact normal force. This limitation places upper and lower bounds on the constraint force variable: $\boldsymbol{\lambda}_{\text{lo}} \leq \boldsymbol{\lambda} \leq \boldsymbol{\lambda}_{\text{hi}}$, allowing constrained bodies to accelerate without bounds if the force necessary to hit the acceleration target falls outside of the limits. In ODE, the result is three possible conditions to satisfy a constraint:

1. $\boldsymbol{a}_i \boldsymbol{\lambda} = w_i$ with $\lambda_i \in [\lambda_{i\text{lo}}, \lambda_{i\text{hi}}]$,
2. $\boldsymbol{a}_i \boldsymbol{\lambda} > w_i$ with $\lambda_i = \lambda_{i\text{lo}}$, or
3. $\boldsymbol{a}_i \boldsymbol{\lambda} < w_i$ with $\lambda_i = \lambda_{i\text{hi}}$

[5] These values are presented without derivation in the ODE user-manual: `http://ode-wiki.org/wiki/index.php?title=Manual:_All#How_To_Use_ERP_and_CFM`. Note that our formulation of β has an extra h in the denominator which is added automatically by ODE.

bioRxiv preprint doi: https://doi.org/10.1101/2020.08.23.262048; this version posted August 24, 2020. The copyright holder for this preprint (which was not certified by peer review) is the author/funder, who has granted bioRxiv a license to display the preprint in perpetuity. It is made available under aCC-BY-NC-ND 4.0 International license.

where $-\infty \leq \lambda_{i\text{lo}} \leq 0 \leq \lambda_{i\text{hi}} \leq \infty$.

A linear solver cannot handle these extra conditions on the constraint forces. To solve this type of system, physics engines employ a mixed Linear Complementarity Problem (mLCP) solver. ODE offers two different solving methods for satisfying constraints under limited-force conditions. One method, known as Projected-Gauss-Seidel, solves constraints iteratively and accumulates the effects [45]. Iterative methods tend to be faster, but also tend to be inaccurate when the system is near-singular or ill-conditioned. Simulated humanoid systems, particularly with two feet on the ground, tend to behave badly with this faster solver. The slower, pivot-based method, follows the algorithm presented by Baraff [46]. Baraff's method is still easily fast enough for our purposes.

Each row in matrix $\boldsymbol{A}$ represents a constraint. The corresponding values of $\boldsymbol{w}$ and $\boldsymbol{\lambda}$ represent a "target" acceleration along the degree of freedom constrained by that row and the generalized force used to achieve it. For the ith row of $\boldsymbol{A}$, the diagonal element, a_{ii}, behaves like the inverse mass of the constraint. A force, λ_i, imposes an acceleration of $a_{ii}\lambda_i = w_i$ within the constraint error-space. The rest of the elements in a row of $\boldsymbol{A}$ encode the force's effects on other constraint dimensions. A change in the ith constraint force λ_i affects the jth constraint space by accelerating it according to $\delta w_j = a_{ij}\delta\lambda_i$. The order of the constraints is arbitrary and they can be rearranged as long as every row-swap is accompanied by the corresponding column-swap that maintains the proper symmetry.

Baraff's solving algorithm (based on Dantzig's simplex method) takes advantage of this arbitrary ordering by dividing constraints into different sets: a satisfied set S, a limited set N, and an unaddressed set U. All constraints fit into one of these categories. The first step in finding a solution is to reorder and satisfy all the unlimited constraints, without considering the rest, using a basic linear solver. The resulting system looks like

$$\begin{bmatrix} \boldsymbol{A}_{11} & \boldsymbol{A}_{12} \\ \boldsymbol{A}_{12}^{\text{T}} & \boldsymbol{A}_{22} \end{bmatrix} \begin{bmatrix} \boldsymbol{\lambda}_1 \\ \boldsymbol{0} \end{bmatrix} = \begin{bmatrix} \boldsymbol{w}_1 \\ \boldsymbol{A}_{12}^{\text{T}}\boldsymbol{\lambda}_1 \end{bmatrix} \tag{16}$$

Set S holds the rows of $\boldsymbol{A}_{1i}$. Set U holds the rest. At this point it helps to look at some figures to see what is going on. Each constraint's target conditions can be represented as a piecewise line through force-acceleration space (Fig 13). We will call this multi-segmented line the target manifold for each constraint. Viewing constraints this way is another contribution of this work. The diagonal element of $\boldsymbol{A}$ associated with the constraint gives the slope of a line through the origin that represents the relationship between force (λ) and actual acceleration (A_{ii} is the effective inverse-mass of the ith constraint). The solver seeks to find a joint solution so that, for all rows of $\boldsymbol{A}$, the pairs of (λ_i, w_i) fall on the acceptable manifold. Forces from other constraints move the entire manifold up or down relative to the origin.

The β parameter takes the horizontal portion of the target manifold and tilts it so that when bigger forces are used, there is a lower target acceleration. Hence the constraint is spring-like. The vertical portions of the constraint represent places where the constraint has hit its force limits. No additional force can be applied by that constraint; so the acceleration must be allowed to increase freely. Otherwise, the constraint would be "obligated" to apply more force to try to get closer to its target acceleration.

Constraints are addressed one-at-a-time. When dealing with ground contact force without softened constraints, once the solver found a sufficient force to keep a body from penetrating the ground, any remaining ground contact constraints would have nothing to do, resulting in inappropriate distribution of ground forces. With spring-like constraints, if one contact

bioRxiv preprint doi: https://doi.org/10.1101/2020.08.23.262048; this version posted August 24, 2020. The copyright holder for this preprint (which was not certified by peer review) is the author/funder, who has granted bioRxiv a license to display the preprint in perpetuity. It is made available under aCC-BY-NC-ND 4.0 International license.

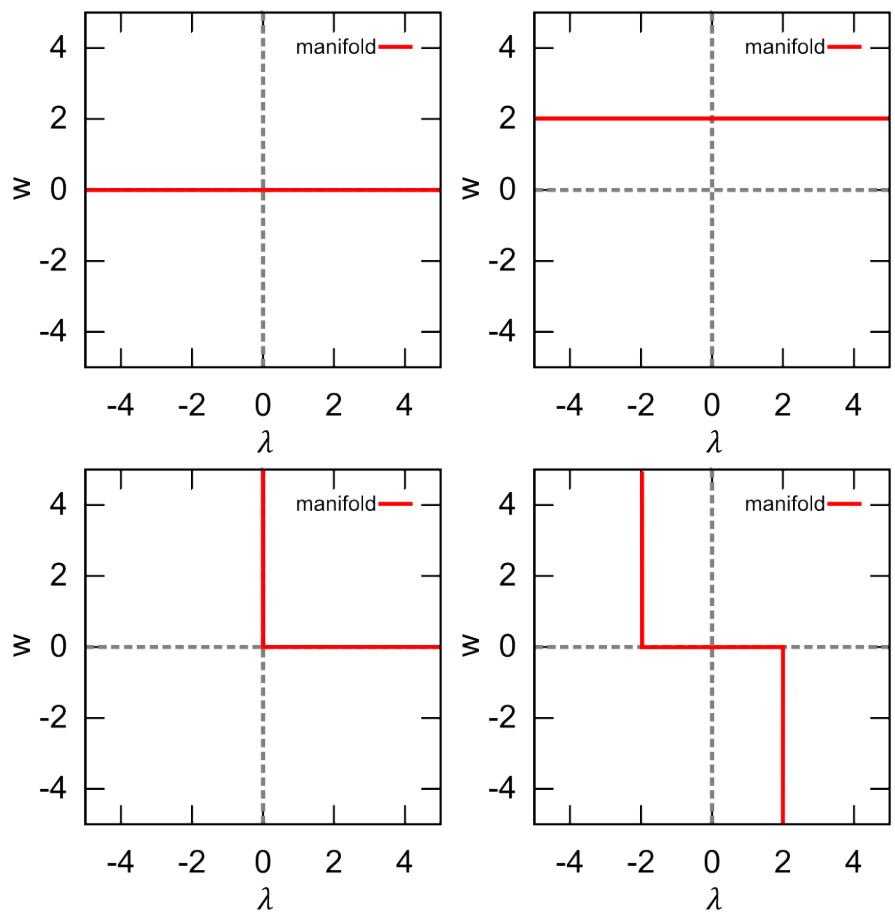

Fig 13. Each constraint on a single degree of freedom can be thought of as a monotonically decreasing, piece-wise linear target manifold through acceleration-force space.

constraint supporting a body reaches its target force/acceleration, a second, redundant contact constraint will see whatever distance remains between the current acceleration and the target. Forces applied by the second constraint attempting to reach its target push the target manifold of the first constraint toward the origin. The force required to achieve the first constraint's target decreases until the forces balance appropriately. The balancing forces make it possible to more accurately compute inverse dynamics forces.

The algorithm for solving the mLCP progresses through each unaddressed constraint, one at a time, and finds the change in forces that will satisfy the new constraint without moving any of the current constraints off their piecewise target. Each iteration of the algorithm draws a new constraint from the unaddressed set U and addresses the change in force, λ, that will satisfy the new row without pushing any previously addressed rows off their manifold, until the new row can be added to S or N. In the process other rows may change between sets S and N, but each row remains on its target manifold in acceleration/force space.

Consider this partitioned matrix:

$$\begin{bmatrix} \boldsymbol{A}_{11} & \boldsymbol{A}_{12} & \boldsymbol{a}_{13} \\ \boldsymbol{A}_{12}^{\mathrm{T}} & \boldsymbol{A}_{22} & \boldsymbol{a}_{23} \\ \boldsymbol{a}_{13}^{\mathrm{T}} & \boldsymbol{a}_{23} & a_{33} \end{bmatrix} \begin{bmatrix} \boldsymbol{\lambda}_1 \\ \boldsymbol{\lambda}_2 \\ 0 \end{bmatrix} = \begin{bmatrix} \boldsymbol{w}_1 \\ \boldsymbol{v}_2 \\ v_3 \end{bmatrix} \tag{17}$$

bioRxiv preprint doi: https://doi.org/10.1101/2020.08.23.262048; this version posted August 24, 2020. The copyright holder for this preprint (which was not certified by peer review) is the author/funder, who has granted bioRxiv a license to display the preprint in perpetuity. It is made available under aCC-BY-NC-ND 4.0 International license.

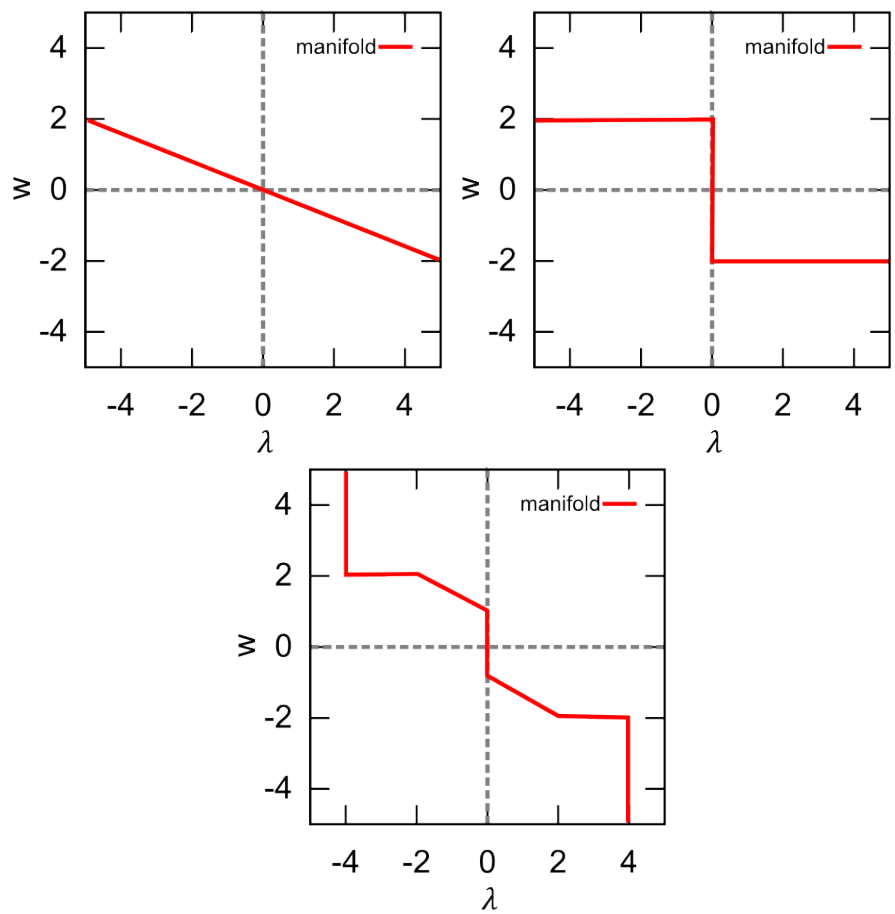

Fig 14. Adding a small value to the diagonal elements of the projected inverse mass matrix turns the constraint into a spring. Viewing constraints as piecewise linear targets provides insights into how to make more complicated constraints consisting of additional piecewise segments.

Adding a new force, λ_3, will change the accelerations of the other constraints. Accelerations of constraints at their limit are allowed to change, but those in set S must remain at their target. So we find the $\delta\lambda_3$ that moves v_3 toward w_3 and find the simultaneous $\delta\boldsymbol{\lambda}_1$ that keeps constraints in S satisfied. The constraint force takes the largest step that will not push any row out of its set. This step will either satisfy the constraint or move another constraint to an intersection point on its manifold. We then pivot the sets around and continue until all of our rows are in S or N. For additional detail, see [46].

Recognizing that the solver deals with each constraint target as a piecewise linear manifold provides useful insight into how the simulation mechanism can be improved. One obvious extension is to increase the number of linear segments in the target manifold beyond three (Fig. 14). This innovation becomes obvious when constraints are considered as target manifolds rather than Lagrange multipliers. With a multi-segment target manifold, it is possible to create a spring-like constraint that is loose near its setpoint, but then becomes stiffer.

We can make spring constraints that get more or less stiff as additional force is required. We can also introduce constraints with "deadzones" in their PD control (Fig. 14). This type of

bioRxiv preprint doi: https://doi.org/10.1101/2020.08.23.262048; this version posted August 24, 2020. The copyright holder for this preprint (which was not certified by peer review) is the author/funder, who has granted bioRxiv a license to display the preprint in perpetuity. It is made available under aCC-BY-NC-ND 4.0 International license.

constraint is particularly interesting because it allows us to introduce controllers that only come into play when a dimension of interest drifts out of an acceptable range. This type of controller takes inspiration from the idea of "uncontrolled manifolds" in human motor control theory [47]. With this constraint acting as a controller, if a perturbation will not hurt performance, the controller does nothing.

From deadzone controllers, we can introduce novel constraints with secondary targets. A constraint whose forces and accelerations fall within acceptable tolerances has flexibility to "help" another constraint that has reached its limit. For example, we can specify a target range for the knee, hip, and ankle joints of a simulated character. When these leg joints fall within their stated ranges, they can be allowed to pursue a secondary goal such as keeping the torso upright or at a given height. This type of constraint can serve as a method for reducing the need for unrealistic residual forces. Removing residual forces implies deviating from original kinematic data. Constraints with secondary targets make it intuitive and clear how this deviation will occur can be extremely beneficial when using the simulation engine for analyzing or synthesizing movement data. We have created and submitted code for allowing controller constraints with a deadzone in acceleration space. [6]

Acknowledgments

Thanks to John Matthis and Leif Johnson for helpful discussions. This research was supported by NSF grant CNS1446578

References

1. Daniel M Wolpert and Michael S Landy. Motor control is decision-making. *Curr. Opinion in Neurobiology*, 22:1–8, 2012.

2. Victor Brian Zordan and Jessica K Hodgins. Motion capture-driven simulations that hit and react. *Proceedings of the 2002 ACM SIGGRAPH/Eurographics symposium on Computer animation*. 89–96, ACM, 2002.

3. Norman I Badler, Cary B Phillips, and Bonnie Lynn Webber

   Simulating humans: computer graphics animation and control *Oxford University Press*, 1993.

4. Auke Jan Ijspeert, Alessandro Crespi, Dimitri Ryczko, and Jean-Marie Cabelguen. From swimming to walking with a salamander robot driven by a spinal cord model *Science*, 315:1417-1419, 2007.

5. John Schulman, Jonathan Ho, Cameron Lee, and Pieter Abbeel.

   Learning from demonstrations through the use of non-rigid registration *Robotics Research*, Springer, 339–354, 2016.

[6] Full implementation of secondary targets for constraints is still in progress. It promises to be useful for creating intelligent constraint-based controllers.

bioRxiv preprint doi: https://doi.org/10.1101/2020.08.23.262048; this version posted August 24, 2020. The copyright holder for this preprint (which was not certified by peer review) is the author/funder, who has granted bioRxiv a license to display the preprint in perpetuity. It is made available under aCC-BY-NC-ND 4.0 International license.

6. Damien M. Callahan, Brian R. Umberger and Jane A. Kent-Braun. A Computational Model of Torque Generation: Neural, Contractile, Metabolic and Musculoskeletal Components. *PLoS ONE*, 8:1-11, 2013.

7. Gerald E. Loeb and GeorgeA.Tsianos. Major remaining gaps in models of sensorimotor systems *Frontiers in Computational Neuroscience*, 9:1-11, 2015

8. Tom Erez, Yuval Tassa, and Emanuel Todorov.

   Simulation tools for model-based robotics: Comparison of Bullet, Havok, MuJoCo, ODE and PhysX *Robotics and Automation (ICRA), 2015 IEEE International Conference on*, 4397–4404, 2015.

9. Diana Burk, James N. Ingram, David W. Franklin, Michael N. Shadlen and Daniel M. Wolpert. Motor Effort Alters Changes of Mind in Sensorimotor Decision Making. *PLoS ONE*, 9:1-10, 2014.

10. A. D. Kuo and J. M. Donelan. Dynamic Principles of gait and their clinical implications. *Physical Therapy*, 90:157-174, 2010.

11. W. M. Land, D A. Rosenbaum and C. Seegelke and T. Schack. Whole-body posture planning: Prospective and retrospective effects. *Acta Psychologica*, 144:298-307, 2013.

12. David A. Rosenbaum, Michael Brach and Andrei Semenov. Behavioral ecology meets motor behavior: Choosing between walking and reaching paths. *Journal of Motor Behavior*, 43:131-136, 2011.

13. Leif Johnson and Dana H Ballard. Efficient Codes for Inverse Dynamics During Walking. *AAAI*, 343–349, 2014.

14. J. M. Cooper and D. H. Ballard Realtime, Physics-Based Marker Following *In Motion in Games*, 350-361, 2012.

15. Joseph Cooper Analysis and Synthesis of Bipedal Humanoid Movement: A Physical Simulation Approach *University of Texas at Austin*, 350-361, 2013.

16. Adam G Kirk, James F O'Brien and David A Forsyth. Skeletal parameter estimation from optical motion capture data *IEEE Computer Society Conference on Computer Vision and Pattern Recognition*, 2:782–788, 2005

17. Edilson De Aguiar, Christian Theobalt and Hans-Peter Seidel. Automatic learning of articulated skeletons from 3D marker trajectories *Advances in Visual Computing*, 485–494, 2006

18. Emel Demircan, Luis Sentis, Vincent Sapio and Oussama Khatib Human Motion Reconstruction by Direct Control of Marker Trajectories *Advances in Robot Kinematics: Analysis and Design*, 263–272, 2008

19. Victor Brian Zordan and Nicholas C. Van Der Horst Mapping optical motion capture data to skeletal motion using a physical model *Proceedings of the 2003 ACM SIGGRAPH/Eurographics symposium on Computer animation*, 6:245–250, 2003

bioRxiv preprint doi: https://doi.org/10.1101/2020.08.23.262048; this version posted August 24, 2020. The copyright holder for this preprint (which was not certified by peer review) is the author/funder, who has granted bioRxiv a license to display the preprint in perpetuity. It is made available under aCC-BY-NC-ND 4.0 International license.

20. Torrence D. J. Welch and Lena H. Ting. Mechanisms of Motor Adaptation in Reactive Balance Control. *PLoS ONE*, 9, 2014.

21. Herman van der Kooij, Edwin van Asseldonk and Frans C.T. van der Helm. Comparison of different methods to identify and quantify balance control. *TJournal of Neuroscience Methods*, 145:175-203, 2005.

22. Luis Sentis, Jaeheung Park, and Oussama Khatib. Compliant control of multi-contact and center of mass behaviors in humanoid robots. *IEEE Transactions in Robotics*, 26(3):483–501, June 2010.

23. Christian D Remy and Darryl G Thelen. Optimal estimation of dynamically consistent kinematics and kinetics for forward dynamic simulation of gait. *Journal of biomechanical engineering*, 2009.

24. Mark L. Latash. *Optimal estimation of dynamically consistent kinematics and kinetics for forward dynamic simulation of gait.* Journal of biomechanical engineering 2009

25. L. H. Ting and J. M. Macpherson. A limited set of muscle synergies for force control during a postural task. *Journal of Neurophysiology*, 93:609-613, 2005.

26. L. H. Ting. Dimensional reduction in sensorimotor systems: a framework for understanding muscle coordination of posture. *Progress in Brain Research*, 165:299-613, 2007.

27. R. Iyer and D. H. Ballard. Basis function models of muscle movement. *BIOROB*, Tokyo, Japan, 2010.

28. R. Iyer and D. H. Ballard. Basis function muscle models of human movement. *Progress in Motor Control*, Cincinnati, Ohio, 2011.

29. R. Iyer and D. H. Ballard. Humanoid muscle movement representation. *Humanoids 2011*, Bled, Slovenia, 2011.

30. Nicholai Bernstein. The co-ordination and regulation of movement. *London: Pergamon*, 18:58-59, 1998.

31. Mark L. Latash. *Synergy.* Oxford University Press, USA, 2008.

32. C. G. Atkeson and S. Schaal. Robot Learning From Demonstration. In *Machine Learning: Proceedings of the Fourteenth International Conference (ICML '97)*, 12–20, 1997.

33. Jan Awrejcewicz, G. Kudra, and B. Zagrodny. Nonlinearity of muscle stiffness. *Theoretical and Applied Mechanics and Letters*, 2, 2012.

34. Reza Shadmehr and Michael A. Arbib. A mathematical analysis of the force-stiffness characteristics of muscles in control of a single joint system. *Biological Cybernetics*, 66:463–477, 1991.

35. Nicholai Bernstein. The co-ordination and regulation of movement. *London: Pergamon*, 1967.

bioRxiv preprint doi: https://doi.org/10.1101/2020.08.23.262048; this version posted August 24, 2020. The copyright holder for this preprint (which was not certified by peer review) is the author/funder, who has granted bioRxiv a license to display the preprint in perpetuity. It is made available under aCC-BY-NC-ND 4.0 International license.

36. Anatol G. Feldman and Mindy F. Levin. *Progress in Motor Control*, volume 629 of *Advances in Experimental Medicine and Biology*, chapter The Equilibrium-Point Hypothesis – Past, Present and Future. Springer, 2009.

37. François Faure, Gilles Debunne, Marie-Paule Gascuel and Frank Multon. Dynamic analysis of human walking. *In Eurographics Workshop on Computer Animation and Simulation*, 8:53–65, 1997.

38. F. Sebastian Grassia. Practical parameterization of rotations using the exponential map. *Journal of graphics tools*, 3:29–48, Taylor & Francis, 1998.

39. Samuel R Buss. Accurate and efficient simulation of rigid-body rotations. *Journal of Computational Physics*, 164:377–406 Elsevier, 2000.

40. Roy Featherstone. Rigid body dynamics algorithms. *Journal of Computational Physics*, 49, Springer Berlin, 2008.

41. Russell Smith. Constraints in Rigid Body Dynamics. *Best of Game Programming Gems*. Charles River Media, 2008.

42. J. Baumgarte. Stabilization of constraints and integrals of motion in dynamical systems. *Computer methods in applied mechanics and engineering*, 1:1–16. Elsevier, 1972.

43. Cornelius Lanczos. The variational principles of mechanics. Courier Dover Publications, 1970.

44. Open Dynamics Engine. ODE User Manual. *http://ode-wiki.org/wiki/*. [Online; accessed 19-July-2013], 2013.

45. Erin Catto. Iterative dynamics with temporal coherence Crystal Dynamics, Menlo Park, California, 2005.

46. David Baraff. Fast contact force computation for nonpenetrating rigid bodies. *Proceedings of the 21st annual conference on Computer graphics and interactive techniques*, SIGGRAPH '94, 23–34. ACM, New York, NY, USA, 1994.

47. J. P. Scholz and Gregor Schöner. The uncontrolled manifold concept: identifying control variables for a functional task. *Experimental Brain Research*, 126:289-306. Springer-Verlag, 1999.

48. M. Tournier, X. Wu, N. Courty, E. Arnaud, and L Revéret. Motion Compression using Principal Geodesics Analysis. *Computer Graphics Forum*, 28:355–364. Blackwell Publishing Ltd, 2009.

49. Yuval Tassa, Tom Erez and Emanuel Todorov. Synthesis and stabilization of complex behaviors through online trajectory optimization. *IROS*, 4906-4913, 2012.

50. Alberto Ranavolo, Romildo Don, Angelo Cacchio, Mariano Serrao, Marco Paoloni, Massimiliano Mangone and Valter Santilli. Comparison Between Kinematic and Kinetic Methods for Computing the Vertical Displacement of the Center of Mass During Human Hopping at Different Frequencies. *Journal of Applied Biomechanics*, 24:271-279, 2008.

bioRxiv preprint doi: https://doi.org/10.1101/2020.08.23.262048; this version posted August 24, 2020. The copyright holder for this preprint (which was not certified by peer review) is the author/funder, who has granted bioRxiv a license to display the preprint in perpetuity. It is made available under aCC-BY-NC-ND 4.0 International license.

51. Helen Huang, Rodger Kram and Alaa A. Ahmed. Reduction of Metabolic Cost during Motor Learning of Arm Reaching Dynamic. *Journal of Neuroscience*, 32:2182–2190, 2012.

52. David W. Franklin, Etienne Burdet, Rieko Osu, Mitsuo Kawato and Theodore E. Milner. Functional significance of stiffness in adaptation of multijoint arm movements to stable and unstable dynamics. *Experimental Brain Research*, 151:145-157, 2003.

53. David W. Franklin, Gary Liaw, Theodore E. Milner, Rieko Osu, Etienne Burdet and Mitsuo Kawato. Endpoint Stiffness of the Arm Is Directionally Tuned to Instability in the Environment. *The Journal of Neuroscience*, 27:7705-7716, 2007.

54. A. V. Hill. First and last experiments in muscle mechanics. Cambridge University Press, 1970.

55. D.F.B. Haeufle, M. Günther, A. Bayer and S. Schmitt. Hill-type muscle model with serial damping and eccentric force–velocity relation. *Journal of Biomechanics*, 47:1531-1536, 2014.

56. Herre Faber, A. J. Van Soest and Dinant A. Kistemaker, Inverse dynamics of mechanical multibody systems: An improved algorithm that ensures consistency between kinematics and external forces. *PloS one*, USA, 2018.

57. Kai Ding, Libin Liu, Michiel van de Panne and KangKang Yin. Learning Reduced-Order Feedback Policies for Motion Skills. *ACM SIGGRAPH* 2015.

58. Xiuping Mu. Dynamics and motion of a five link robot walking in the sagittal plane. *The University of Manitoba* 2004.

59. Marc Raibert. Legged Machines that Run. *MIT Press* Cambridge, MA, USA, 1986.

60. Anatol Feldman. Once more on the equilibrium-point hypothesis (lambda model) for motor control. *Journal of motor behavior*, 18:17-54, 1986.

61. Luc P.J. Selen and Peter J. Beek and Jaap H. van Dieën. Can co-activation reduce kinematic variability? A simulation study. *Biological Cybernetics*, 93:373-381, 2005.

62. J. S. Matthis and B. R. Fajen. Humans exploit the biomechanics of bipedal gait during visually guided walking over complex terrain. *Proceedings of the Royal Society of London B: Biological Sciences*, 2013.

63. Justus D. Ortega, Leslie A. Fehlman and Claire T. Farley. Effects of aging and arm swing on the metabolic cost of stability in human walking. Journal of biomechanics, 2008.